Frequency of exceptional Nile flood events as an indicator of Holocene hydro-climatic changes in the Ethiopian Highlands

Carlo Mologni[1-6] *, Marie Revel[1], Cécile Blanchet[2], Delphine Bosch[3], Anne-Lise Develle[4] François Orange[5], Luc Bastian[1], Lamya Khalidi[6], Emmanuelle Ducassou[7], Sébastien Migeon[1-8]

[1]Université Côte d'Azur, CNRS, Observatoire de la Côte d'Azur, IRD, Géoazur, 06905 Sophia Antipolis, France

[2] GFZ Potsdam, Department of Climate and Landscape Dynamics, Telegrafenberg, 14743 Potsdam

[3] Géosciences Montpellier, CNRS UMR-5243, Université Montpellier II, 34095 Montpellier, France

[4]Université Grenoble Alpes, Université Savoie Mont Blanc, CNRS, EDYTEM, 73000 Chambéry, France

[5] Université Côte d'Azur, CCMA, 06100, Nice, France

[6] Université Côte d'Azur, CNRS, CEPAM – UMR 7264, 06300 Nice, France

[7] CNRS UMR-5805 EPOC – OASU, Université de Bordeaux, Site de Talence - Bâtiment B18N, 33615 Pessac, France

[8] Sorbonne Université, UFR939, 06230 Villefranche-sur-Mer, France.

*corresponding author: mologni@geoazur.unice.fr

Abstract

Climate conditions in Africa have varied substantially during the Late Quaternary with alternating humid and arid periods controlled mainly by the African monsoonal regime. However, the duration and termination of the last African Humid Period (14-6 ka BP) and its internal climatic variability are still debated. Using a laminated sequence from the Nile Deep-Sea Fan, we reconstruct for the first time the monsoon-induced frequency of exceptional Nile floods at centennial resolution during the African Humid Period. By combining sedimentological, geochemical and microscopic tools and comparing our record with two proximal piston cores and with regional paleoclimatic records, we show: **a)** the occurrence of recurrent high-energy floods between 10.1 and 9 ka BP, during the height of the African Humid Period; **b)** a shift in the hydro-climatic regime as early as 9 ka BP, with a progressive reduction in flood frequency and magnitude until 8.2 ka BP, likely related to a southward migration of the monsoon rainfall belt; **c)** a drastic reduction of flood activity between 8.2 and 7.8 ka BP; **d)** an unstable Ethiopian-Nile hydrological system from 7.8 ka BP, followed by a further decrease in river runoff until ~4 ka BP. The occurrence of a stepwise hydro-climatic deterioration over the Ethiopian Highlands from ~9 ka BP brings

into question the climatic linkages and feedbacks between low and high latitudes during the Early to Mid-Holocene and in particular around the 8.2 ka BP North Atlantic cooling event. Our unique record of flood frequency at centennial-resolution therefore allows us to draw new insights on fluvial and geomorphic feedbacks of the Nile hydrologic system to monsoonal regimes during a period of major environmental shifts.

Keywords

1. Introduction

Monsoons are the dominant seasonal mode of climate variability in the tropics, acting as the main driver of climate worldwide. At present, the tropics concentrate the maximum amount of energy and redistribute it in the form of air and moisture masses to subtropical latitudes between 30°N and 30°S. Hydro-climatic conditions in the current Sahel area (Fig. 1b) have varied in the past following a precessional pacing (i.e., every 21,000 years; Mohtadi et al., 2016). Periods that were more humid in the past compared with present-day conditions have been attributed to the northward migration of the rainfall belt associated with the Inter Tropical Convergence Zone (ITCZ; Mohtadi et al., 2016). This migration is governed by precession-driven insolation changes and modulated by the eccentricity (deMenocal et al., 2000; Gasse, 2000; Rossignol-Strick et al., 1982; Skonieczny et al., 2019). Past humid periods were characterized by enhanced discharge and sediment export from the large African river systems to surrounding ocean margins. The most recent period of more intense rainfall, the African Humid Period (AHP: from ~14 to ~6 ka BP; Shanahan et al., 2015), led to the expansion of continental water bodies (Gasse, 2000), the development of vegetation cover over the present-day Sahelian-Saharan desert (Hopcroft et al., 2017) and very high riverine-induced terrigenous inputs. Many recent studies conducted at high temporal resolution (100 years) in lake and deltaic sediment records across the East African Rift System and over the north African continental margins suggest that gradual long-term monsoon oscillations (controlled by external orbital forcing) were often punctuated by millennial-scale episodes of hyper aridity (Bastian et al., 2017; Chalié and Gasse, 2000; Costa et al., 2014; Foerster et al., 2012; Tierney and deMenocal, 2013; Verschuren et al., 2009).

The most recent arid episodes occurred during the AHP and at the onset of the AHP (8.2 and 12.8 ka BP), coinciding with the melting of icebergs from the Laurentide ice sheet into the Arctic (Collins et al., 2017, 2011). It has been proposed that the reduction of Atlantic thermohaline circulation could have induced a reduction of African monsoon activity (Mulitza et al., 2008). In order to understand the mechanisms linked to these abrupt climate changes between low and high latitudes, it is crucial to work on natural archives with a centennial to decadal temporal resolution.

60 The main goal of this work is to investigate Nile river discharge over the last ~10.3 thousand years at a

61 centennial time resolution, with the aim of documenting the internal dynamics of the AHP in East

62 Africa. A particular focus will be set on the 8.2 ka BP arid event, to better understand the timing,

63 mechanism and feedback of African monsoon activity in the Ethiopian-Nile basin.

64 Sediment deposition in deltas is dominated by terrigenous material delivered from flooding rivers and

65 is highly sensitive to changes in precipitation rate and the extension of vegetation cover in drainage

66 basins. The sediment records preserved on the Nile Deep-Sea Fan (NDSF) provide suitable archives for

67 reconstructing past continuous climate variations (Ducassou et al., 2009). Previous studies on the

68 NDSF have demonstrated that past humid periods were systematically accompanied by higher

69 deposition rates and enhanced terrigenous supply, reflecting strong physical erosion and transport

70 processes from the Ethiopian Highlands related to African monsoon activity (Blanchet et al., 2014;

71 Ducassou et al., 2009; Krom et al., 2002; Revel et al., 2010; Revel et al., 2015). In addition, the

72 provenance of particles exported to the NDSF has been inferred from the application of Nd and Sr

73 radiogenic isotopes in sediment cores (See section 2.2).

74 Over the NDSF, the variability of lithological facies includes pelagites/hemipelagites, turbidites,

75 debrites, slide/slump deposits and clastic muds (Ducassou et al., 2009, 2008, 2007; Migeon et al.,

76 2010). During strong flood events, fine- to coarse-grained beds named hyperpycnites can be deposited

77 at ocean and sea margins (Mulder et al., 2003, 2001; Parsons et al., 2001). However, in the NDSF, Nile

78 flood events seem to be recorded through the emplacement of the so-called "clastic-mud beds"

79 (Ducassou et al. 2008; Revel et al. 2010; Blanchet et al. 2013). The deposition of these beds is

80 explained by the reconcentration of surface plumes originating from terrigenous river discharge by

81 convective processes leading to the formation of hyperpycnal flows at depth (Ducassou et al., 2008;

82 Parsons et al., 2001).

83 In this study, we focus on well-preserved turbidite beds located in the Western Province of the NDSF

84 (MD04-2726 core, Fig. 1), that we interpret to be a potential instantaneous and direct record of the

85 Nile-river floods during the AHP, related to African paleo-monsoon activity.

86 Integrating multiproxy sedimentological and geochemical (major elemental and Nd isotopes) data, we

87 address four challenges: **a**) distinguishing between beds deposited by hyperpycnal flows and those

88 induced by failure-triggered gravity flows or by density convective processes (clastic-mud beds) along

89 the Rosetta Canyon and the continental slope; **b**) confirming the coherency of these hyperpycnal-flow

90 deposits over the western NDSF by comparing them with similar laminated and well-dated records in

91 the Rosetta System (MS27PT and P3622-33 cores; Revel et al., 2015; Blanchet et al., 2013,

92 respectively); **c**) characterising the frequency and magnitude of Nile paleo-floods over the last 10.1

93 kyr; and **d**) finally, discussing the meaning of Nile-flood frequencies at centennial resolution and their

94 links with paleo-monsoon activity during the AHP, with a particular focus on the Early to Mid-Holocene

95 and on the the 8.2 ka BP hyper-arid event (Rohling and Pälike, 2005).

96 These results will be of interest to better constrain identification of hyperpycnal-flow deposits within

97 mud-prone turbidite systems similar to the Nile Deep-Sea Fan and to better constrain African paleo-

98 monsoon dynamics for integration within broader climate modelling.

99 ## 2. Regional settings

100 ### 2.1 The NDSF Western Province morphology

101 Core MD04-2726 was collected in the upper part of the Rosetta Turbidite System, located on the

102 western NDSF (Ducassou et al., 2009; Mascle et al., 2006), off the Rosetta branch of the Nile subaerial

103 delta (Fig. 1a). Here, the continental shelf is about 30 km wide, and the head of the Rosetta Canyon

104 lies on the outer continental shelf at a water depth of about 70 m (Fig. 1a). It is about 25 km long and

105 200-250 m deep, and is straight following the main slope angle of the continental slope. In cross

106 section, the Rosetta Canyon is characterized by U- to poorly-developed V-shaped profiles where a

107 large number of small-scale failures affected the canyon flanks (Fig. 1a). The Rosetta Canyon connects

108 to a meandering channel-levee system named DSF6, which was initiated during Marine Isotopic Stage

109 3 (MIS 3) (Ducassou et al., 2009) and potentially recorded the Holocene activity of the Nile flood-

110 induced inputs.

111

2.2 The NDSF Western Province sediment sources

113 The sedimentary provenance of terrigenous material in the western NDSF can be characterized

114 through its neodymium isotopic signature (εNd) (Bastian et al., 2017; Blanchet et al., 2014; Blanchet,

115 2019; Migeon et al., 2010; Revel et al., 2010; Weldeab et al., 2002). Since the Nile basin encompasses

116 the Precambrian African basement as well as the Cenozoic Ethiopian traps, which have contrasting Nd

117 isotopic compositions, geochemical studies on its sediment loads allow us to distinguish between the

118 sources of the material (Fig. 1b). 96% of the particles deposited in the NDSF today are estimated to

119 originate from the Blue Nile and Atbara rivers and only 4% from the White Nile (Be'eri-Shlevin et al.,

120 2018; Garzanti et al., 2015; Padoan et al., 2011). The Bahr el Jebel and Victoria-Albert Nile-derived

121 fluvial muds are characterized by εNd(0) ≈-25 (Padoan et al., 2011), whereas the White Nile mud

122 reaching Khartoum could have a Saharan Metacraton imprint with εNd around -13 (Fig. 1b; Skonieczny

123 et al., 2011). Aeolian dust from the western to central Saharan region are characterized by relatively

124 constant values of εNd ranging between -10 to -15 (Grousset and Biscaye, 2005; Scheuvens et al.,

125 2013).

126 Thus, temporal changes in both Nd signature and sedimentation rate from sedimentary records in the

127 NDSF allow us to track past temporal changes in relative proportions of detrital sediment originating

128 from the Ethiopian Traps located in tropical latitudes between 5°N to 15 °N (εNd > 0), the Central

129 Africa Craton located in equatorial latitude (εNd ≈ −30), and the Saharan Metacraton located in the

130 present Sahara (Abdelsalam et al., 2002) and which is an important aeolian dust producer (εNd ≈ −10

131 to −15).

3. Materials and methods

133 The present study is based on the analysis of the MD04-2726 core (N 31°51.00', E 29°47.49') collected

134 during the VANIL campaign (2004). The total MD04-2726 piston core length measures 26.5 m and is

135 composed of 18 sections. Because of the good preservation of the hyperpycnite sequence and

136 according to the aim of this and previous studies (Revel et al. 2015) we focused our investigation on

137 the upper five sections (732 cm; Fig. 2e). The core was extracted on the right-hand levee of the upper

138 Rosetta Channel at a water depth of 1058 m (Fig. 1a), and represents the closest core from the

139 coastline to have been collected on the Nile margin, i.e. <60 km away from the Rosetta-river mouth.

140 This core is characterized by high accumulation rates and thus provides high-resolution temporal

141 information on the links between hydro-climate and erosion processes on continents.

142 Identification of individual depositional beds was based on the integration of various methods

143 including visual description at millimetre scale, grain-size, XRF-CS, Nd isotopic composition and thin-

144 section analyses that are described below.

145 ### 3.1 AMS ^{14}C measurements

146 The age model of the MD04-2726 sequence was constructed using thirty Accelerator Mass

147 Spectrometry (AMS) ^{14}C dates (Tab. 1). In order to improve the age model for core MD04-2726 (Revel

148 et al., 2015), a set of 18 additional radiocarbon ages was obtained (Tab. 1, Fig. 2a). The scarcity of

149 planktonic foraminifera shells in sections III-IV-V precludes the addition of new radiocarbon

150 measurement on biogenic carbonates. We therefore obtained seven new AMS ^{14}C measurements on

151 bulk organic matter (bulk OM) for this part of the core and 11 new AMS ^{14}C measurements of

152 planktonic foraminifera shells in sections I-II-III (Fig. 2, Tab. 1).

153 Calibrated ages were obtained with the OxCal software (v4.3.2, Bronk Ramsey, 2017), while the age-

154 depth modelling was performed using the Bacon software (v3.6.3, Blaauw and Christen, 2011).

155 Conventional ages on foraminifera assemblages were calibrated using the MARINE13 calibration

156 curve, which includes a mean global reservoir correction of 400 yrs (Reimer et al., 2013; Siani, 2001).

157 Paired measurements of AMS ^{14}C of planktonic foraminifera and bulk OM on the same depth interval

158 (658 cm, section V; Tab. 1) allows us to estimate the age reservoir correction of the continental OM.

159 Inversely to classical methods to determine the local age reservoir for marine sediments (Dewar et al.,

160 2012; Reimer et al., 2002; Reimer and Reimer, 2017), we used the calibrated age of planktonic

161   foraminifera (to MARINE13, 9736 cal. yr BP) to determine the apparent age of contemporaneous

162   organic matter (from IntCal13, 8766 cal. yr BP) and calculated the difference to the radiocarbon age of

163   bulk OM (10620 yr BP). The calculated offset of 1854 yr was used as a constant reservoir age to

164   correct all radiocarbon ages on organic matter (Table 1). Owing to the dominantly continental origin of

165   bulk OM in sediments from the NDSF deposited during the African Humid Period (Blanchet et al.,

166   2014; Menot et al., 2020), the ages on bulk OM and on organic macro-remains were calibrated using

167   the IntCal13 curve (Reimer et al., 2013). The reliability of the age model and inherent limitations will

168   be further discussed in section 4.1.

169

170   **3.2 XRF core scanner on soft sediment**

171   X-Ray fluorescence core scanning (XRF-CS) was performed on an Avaatech core scanner at the

172   EDYTEM laboratory (CNRS-Université de Savoie Mont-Blanc). The XRF-CS analyses were performed on

173   core MD04-2726 with a 1 mm sampling step and with a 10 kV voltage (Al, Si, S, K, Ca, Ti, Mn, Fe) for

174   sections I-II (Revel et al. 2015), and with a 10 KV and 30 kV voltage (Al, Si, S, K, Ca, Ti, Mn, Fe; Cu, Zn,

175   Br, Sr, Rb, Zr, Pb) for sections III-IV-V (this study). Each individual power spectrum was transformed by

176   deconvolution into relative contents (intensities) expressed in counts per seconds (cps). In this study

177   we principally used the logs of elemental ratios, following a well-established methodology to

178   circumvent problems associated with the closed-sum constrains (Croudace and Rothwell, 2015; Weltje

179   and Tjallingii, 2008).

180   A principal component analysis (PCA) was performed on geochemical results using the R® software.

181   This statistical procedure uses an orthogonal transformation to convert a set of observations of

182   possibly correlated variables (our elements) into a set of values of linearly uncorrelated variables

183   called principal components (dimensions). This analysis has been thus applied to XRF results in order

184   to decipher sedimentary processes controlling MD04-2726 geochemical variations (Sup. Mat. Fig A.1).

3.3 Particle grain size analysis and LOI

Grain-size analyses were performed using a Coulter-LS2000 following two sampling strategies: **a**) a centimetre-scale sampling step over the total core length (733 cm); **b**) a millimetre-scale sampling step (2 mm) in selected individual beds identified using the mm-XRF major elemental variation and centimetre-resolution grain-size distribution data. To avoid clay flocculation and to dissociate mineral particles, we used sodium hexametaphosphate (NaHMP) and ultrasonic treatment. Sediment was previously decarbonated (HCl, 1 mol), while the organic matter was maintained (no H_2O_2 dissolution), considered as a grain-size marker of river-induced instantaneous deposits. SEM and light microscopic qualitative analyses on this section and on bulk decarbonised sediment (see 3.4 for methodology) showed the near-absence of diatom frustules, which are thus considered as a negligible factor for grain-size measurements and interpretations.

We determined the grain-size of the intercepts for 10%, 50% and 90% of the cumulative grain-size curves (named Q90, Q50 and Q10 values; Folk and Ward, 1957). The ratio Q90/Q10 is used to identify the coarser-grained beds (hyperpycnites) along the studied interval, while the Q90/Q50 ratio and Gaussian curves are used to discriminate between the bed types and to propose a hydrodynamic interpretation.

Loss On Ignition (LOI) was performed on 2 g sediment samples by heating for 24 h at 100°C for residual water and gypsum content and then 4 h at 550°C for organic carbon total content measures (Santisteban et al., 2004).

3.4 Light and Electron Microscopy Analyses

Microscopic analyses were performed on 11 thin sections sampled in selected individual beds (Fig. 3). Thin sections were analysed using the Zeiss Axioskop 40 Pol/ 40 petrographic microscope with UV light used to detect phosphate materials. Pictures of total thin sections presented in this article were obtained from high-resolution transmission scanning in crossed (XPL) and direct polarized light (PPL).

209 Qualitative and semi-quantitative geochemical analysis on uncovered thin sections was performed

210 using scanning electron microscopy (SEM). SEM was also used for the surface textural analyses of

211 quartz grains, following Vos et al. (2014) sampling processing and analysis settings. SEM observations

212 and Energy Dispersive X-Ray spectroscopy (EDX) analyses were carried out with a Tescan Vega3 XMU

213 scanning electron microscope (TESCAN FRANCE, Fuveau, France) equipped with an Oxford X-MaxN 50

214 EDX detector (Oxford Instruments, Abingdon, U.K.). Thin sections were observed and analysed with no

215 prior metal or carbon coating, using the low vacuum mode (N2 pressure ~35 Pa) and at a 20 kV

216 accelerating voltage. Imaging was performed using backscattered electrons. EDX spectra were

217 processed with the Aztec software (version 3.1, Oxford Instruments). Surface textural analyses of

218 quartz grains were performed on 10 to 20 grains for each of the beds identified in thin sections, with a

219 grain-size range between 100 µm to 1 mm, randomly selected under a binocular microscope and then

220 analysed using the SEM. Quartz grains were coated with platinum (3 nm) prior to SEM observations at

221 a 5kV accelerating voltage.

222 ### 3.5 Nd radiogenic isotope analyses

223 Isotope ratios were measured on carbonate-free <63 µm particle size both on hemipelagic and

224 turbidite deposits, using 100 mg of the dried aluminosilicate fraction. Chemical extractions for Nd

225 isotopes were carried out at the Laboratory of Geoscience Montpellier. Samples were leached for 1

226 hour with 1N HCl to dissolve biogenic carbonates. The Fe-Mn oxyhydroxide fraction and organic

227 carbon were removed using 10 ml 1M Hydroxylamine hydrochloride and 10 ml 5% H_2O_2, respectively

228 (Bayon et al., 2002). After leaching, the samples were centrifuged and the supernatant discarded. The

229 remaining sediment was washed three times with ultra-pure water, discarding the supernatant each

230 time to remove the biogenic components and to eliminate any marine Nd isotope signal adsorbed on

231 to the silt-clay fraction. The chemical separation of Nd included a first separation step using AG50W-X-

232 8 cation exchange resin to collect rare earth elements followed by purification of Nd using HDEHP

233 conditioned Teflon columns. Nd isotopes were measured using a Thermo Scientific Neptune Plus MC-

234 ICP-MS from the AETE-ISO geochemical platform (OSU-OREME, Montpellier University). The

235 ^{143}Nd/^{144}Nd isotopic compositions were corrected for internal mass bias using an exponential law and

236 a value of 0.7219 for the ^{146}Nd/^{144}Nd ratio. The external mass bias was corrected using the standard

237 bracketing method using AMES-Rennes and analysing each of the 2 unknowns. During the course of

238 the study AMES-Rennes standards yielded an average 0.511946±6 (2σ, n=10) for the ^{143}Nd/^{144}Nd ratio

239 (Chauvel and Blichert-Toft, 2001). The Nd procedural blank measured during the course of this study

240 was 25 pg. Epsilon Nd values (εNd) were calculated using ^{143}Nd/^{144}Nd = 0.512638 (Bouvier et al.,

241 2008).

4. Results

4.1 Age model, lithology and sedimentation rates

244 According to the age model, the upper 7.3 m of core MD04-2726 span the last 10 kyr, covering the

245 Holocene period (Fig. 2a). Both the range (between 0.2 and 3.5 mm/yr) and the timing of changes in

246 sedimentation rates are coherent with previous reports from nearby archives (Blanchet et al., 2013,

247 Revel et al., 2014, 2015; Hennekam et al., 2015). A large variability in radiocarbon ages (including

248 several reversals) is observed in sections III-IV-V, where the highest sedimentation rates are computed

249 (>1 mm/yr). This is probably related to unaccounted changes in the reservoir age of bulk OM through

250 time, due to varying proportion of terrestrial and marine OM in the sediments as well as to the

251 incorporation of terrestrial OM of varying ages. Complex interplay between storage and erosion

252 processes in fluvial basins can indeed lead to the release of pre-aged OM as old as 2000 yrs, as shown

253 by (Schefuß et al. (2016) for the Congo River. A reservoir age of ~1200 yr has been obtained for a layer

254 dated at ca. 9 ka BP in nearby core P362/2-33 (unpublished results, C. Blanchet), which is 650 yrs

255 younger than the reservoir age of ~1850 yrs obtained for core MD04-2726 at ca. 9.8 ka BP. We

256 therefore consider that uncertainties on radiocarbon ages obtained on bulk OM associated with likely

257 variations in reservoir age through time are in the order of ~500 yrs. For all other ages, uncertainties

258 range between ~30 and ~100 yr, see Table 1). Accounting for these inherent limitations and for the

259 generally lower temporal resolution of regional records, we limit our interpretations to centennial-

260 scale changes.

261 Based on the lithology, four sedimentological intervals were identified in core MD04-2627, depicted

262 here from bottom to top. The first interval lies between 732 and 700 cm and is dated between ~10.3

263 to ~10.1 ka BP (Fig. 2a). It is composed of muddy non-laminated sediment (Fig. 2e). The second

264 interval ranges from 700 to 132 cm and is dated between ~10.1 and ~7.2 ka BP. It is characterized by

265 sandy-silt to silty-mud turbidites and laminated hemipelagic muddy beds, with sedimentation rates

266 between ~1 and ~3.5 mm/yr. The total carbonate content never exceeds 10%. The whole interval

267 corresponds to the Sapropel S1, formed under anoxic bottom-waters conditions which circumventing

268 the bioturbation (Thomson et al., 1999). Thus we observe a high organic content (8-9 %; Fig. 4a), a low

269 Mn/Al values (Fig. 2d) and the lack of bioturbation features. The third interval lies between 132 and 70

270 cm and is dated between ~7.2 and ~5.8 ka BP (Fig. 2a). It represents the transition from sapropelic to

271 pelagic conditions with no turbidite beds, corresponding to the increase of deep and intermediate

272 water ventilation in the Eastern Mediterranean during the termination of the AHP. The fourth interval

273 corresponds to the upper 70 cm and spans the last 5.8 kyr. A reduction of S/Cl (Revel et al., 2015) and

274 two peaks of Mn/Al ratio at 6.8 and 4.3 ka BP mark the reestablishment of Mid-Holocene oxic

275 conditions (Fig 2d; De Lange et al., 2008). This interval has a sedimentation rate of ~0.15 mm/yr (Fig.

276 2a) and consists of yellowish-brown bioturbated pelagic mud devoid of turbidite beds with a great

277 number of planktonic foraminifera.

278

279 ### 4.2 Nd isotopic composition

280 In core MD04-2726, ϵNd values measured on the <63µm silicate fraction range between -2 and -6 and

281 three isotopic trends are distinguished (Fig 2b). Values of ϵNd between -2.5 and -4 are observed

282 between 700 and 400 cm, indicating a larger proportion of particles derived from the Ethiopian Traps.

283 These are followed by values of ϵNd between -4 and -5 observed between 400 and 70 cm. Finally,

284 distinctly low ϵNd values (<-5.5) are measured between 70 to 20 cm in phase with the low values of

285 the Ti/Ca ratio. ƐNd values from turbiditic beds show a systematic offset by ~ +0.6 compared to the

286 hemipelagic facies (Fig. 2b).

4.3 Description of T1 and T2 event-layers

288 The integration of sedimentological and geochemical data allows the identification at millimetre-scale

289 of 102 coarser grain-size beds within the sapropelic interval (~7.2 to ~10.1 ka BP; Fig. 3a). Two types of

290 beds are distinguished: 83 are characterized by an increase of Ti/K, Mn/Al and Q90/Q10 ratio (T1

291 event-layers; Figs. 3, 4, 6) and 19 are characterized by an increase of both the Ti/K and Q90/Q10

292 ratios, without Mn/Al peaks (T2 event-layers; Figs. 3, 5, 6).

4.3.1.   T1 event-layer description

294 T1 event-layers (1 to 6 cm thick) are characterized by a mixed grading, consisting of a basal inverse

295 grading overlaid with an upper normal grading (Fig. 4a). Each T1 bed consists of the superposition of a

296 maximum of 5 facies named I to V from base to top (Fig. 4a).

297 The Facies I (Fig. 4a) consists of a basal coarsening-upward unit with high amounts of clay minerals.

298 Organic-matter micro-remains of continental origin and primary minerals (micas >20 µ) are also

299 present and they coarsen from the bottom to the top of the facies. Facies I is poorly laminated, with

300 an alternation between muddy and silty laminae, the latter thickening upward (Fig. 4a). Together with

301 an inverse grading, Facies I exhibits a gradual upward increase of the Ti/K ratio (Fig. 4a). Facies II is

302 characterized by a sharp basal contact, the disappearance of clay and fine-silt fractions and an

303 increase in grain-size (Fig. 4a). Horizontal parallel laminations are present, with a coarsening-up

304 pattern. Facies II is also characterized by high peaks in Ti/K and Mn/Al ratios, associated with higher

305 Q90/Q10 values. The transition between Facies II and III is gradual. Facies III is the coarsest interval of

306 the T1-type beds. It consists of laminated and cross-laminated intervals (Fig. 4a). Sedimentary

307 structures change upward from horizontal parallel laminations to oblique laminae then back to

308 horizontal laminations. Cross-laminations are interpreted to have been formed during deposition of

309 climbing ripples. Coarse fragments of organic-matter (100-300 µ) are abundant and organised

310   following the sandy laminations (Fig. 4b). Similar distribution and orientation patterns are observed for

311   primary minerals, particularly for micas recognised by their third-order birefringence, by typical

312   phyllosilicate morphology and by EDX elemental analyses (Fig. 4c). Angular and sub-angular grains of

313   quartz present common small to large conchoidal microfractures and V–shaped percussion cracks (Fig.

314   4d). The Ti/K ratio remains high and constant, and the Mn/Al ratio decreases in phase with the coarser

315   material. The transition between Facies III and IV is marked by a sharp contact. Facies IV is a normally

316   graded and laminated interval (Fig. 4a). Horizontal laminations thin and become fine upward.

317   Additional features of Facies IV include an absence of clay and fine-silt material, high amounts of mica

318   minerals and continental organic-matter fragments at the top. Both the Ti/K and Mn/Al ratios increase

319   upward and suddenly decrease at the transition with the overlaying Facies V (Fig. 4a). The transition

320   between Facies IV and V is sharp. Facies V is structureless or poorly-laminated (Fig. 4a). It consists of

321   clay and fine-silt minerals mixed with coarse-grained particles, following a normal grading. Both the

322   Ti/K and Mn/Al ratios decrease upward.

323   The identification of 83 T1 event-layers along the studied laminated interval is therefore based on a

324   combination of Ti/K, Mn/Al and Q90/Q10 peaks. Thicker T1 events are bracketed by Mn/Al peaks (as

325   shown in Fig. 4), while thin T1 events presented only punctual Mn/Al peak, because of analysing

326   resolution effect. The plot of Q90 versus Q50 (Fig. 6a) and grain-size distributions (Fig. 6c) shows two

327   different groups of T1: the first one (T1α) with a Q90max of 100 µm and a Q50max of 12 µm and a

328   bimodal distribution with a dominant mode at 20-30 µm; the second (T1β) with a Q90max of 50-250

329   µm and a Q50max of 12-100 µm and a bimodal distribution with the main well-sorted mode at 50-70

330   µm.

331   *4.3.2.   T2 event-layer description*

332   The beds of type T2 (0.2 to 2 cm thick) are either massive or laminated silty to very-fine sand intervals

333   (Fig. 5a, b, c), with a sharp basal contact, and are not composed of a superposition of subsequent

334   facies. The clay fraction is abundant, while the coarse-grained fraction is well sorted. In contrast to T1

335   event-layers, the few organic-matter fragments follow random organisation and orientation patterns,

336   while rare foraminifera and coccolithophore shells are fragmented (Fig. 5c). Within the whole

337   sapropelic laminated interval (~7 to 10.5 ka BP), beds of type T2 are characterized by more or less

338   pronounced Q90/Q10, Ti/K peaks and by the lack of or very low Mn/Al peaks (Figs. 3b, 6b). All these

339   characteristics suggest a mixed material probably caused by reworked sediments. The plot of Q90

340   versus Q50 is mainly comprised between 60 µm (Q90max) and 40 µm (Q50; Fig. 6b, c) with a grain-size

341   distribution similar to T1α beds (bimodal with a main mode around 20-30 µm).

342   ## 5. Interpretations and Discussion

343   Recurrent Nile exceptional floods trigger high detrital inputs in the Rosetta channel-levee system,

344   resulting in the frequent occurrence of turbidites during the AHP (Fig. 3). Using a multi-proxy method,

345   we are able to distinguish between deposits resulting from "classical" landslide-triggered turbidity

346   currents and hyperpycnal flows (Sec 5.1). We present an estimation of the frequency of T1

347   hyperpycnal event-layers in core MD04-2726 which is compared with two well-dated sediment

348   intervals already identified in cores from the Rosetta System (Sec. 5.2). Finally, from this comparison,

349   we validate the reliability of the Nile flood frequency reconstruction at the scale of the Rosetta System

350   and we propose a robust index of the exceptional flood frequency of the Nile River during the AHP

351   (Sec. 5.3). We then discuss the timing and pattern of this flood frequency in comparison with hydro-

352   climatic data from the Nile basin and East Africa.

353   ### 5.1 - T1 and T2 event-layers: interpretation and formation processes

354   The full T1 event-layers consist of the superposition of five intervals with different types of

355   sedimentary structure and an inverse then normal grading (Fig. 4). In a turbidite system, superposition

356   of an inverse then a normal grading reflects deposition by a waxing (accelerating) then waning

357   (decelerating) flow. First, waxing flows can be generated both by an increasing slope angle and/or by

358   an increasing entrainment of seafloor sediment. Because T1 event-layers were recovered from an

359   almost-flat levee (Figs. 1a, 7b) on which overflow energy should be low, these two hypotheses of

360 waxing flow formation processes are unlikely. Second, waxing flows can be generated at a river mouth

361 during severe floods, such as hyperpycnal flows (Mulder et al., 2001). In this case, the mixed grading

362 together with occurrence of sedimentary structures should record the rapid succession over time of a

363 depletive waxing flow generated during river rise, and a depletive waning flow generated during river

364 fall (Migeon et al., 2001; Mulder et al., 2001). T1 event-layers are similar in both grading and

365 sedimentary structures to hyperpycnites first described in the Var Turbidite System (Migeon et al.,

366 2001; Mulder et al., 2001).

367 Additional observations reinforce the flood-related hypothesis for T1 layers. The fluvial origin of T1

368 layers is supported by both sedimentological and geochemical tracers. First, quartz grains show small

369 to large fresh conchoidal microfractures and V–shaped percussion cracks, typical of fluvial transfer

370 processes (Fig. 5c; Vos et al., 2014). Furthermore, ƐNd values from T1 event-layers (-3 to -2) are

371 systematically higher than corresponding hemipelagic sediments (Fig. 2b), indicating a large

372 proportion of particles deriving from the Ethiopian Traps, which have ƐNd values of 0 to 7 (Fig. 8c, e;

373 Ménot et al., 2020). Higher Ti/K ratios in T1 layers also support a higher contribution of basaltic rocks

374 from the Ethiopian Traps, with primary minerals enriched in Ti, while secondary clay minerals are

375 enriched in K (Croudace and Rothwell, 2015). The good correspondence between Ti/K and Q90/Q10

376 ratios suggests that the Ti/K ratio traces the silt versus clay fraction (Fig. 3b). In addition to coarser

377 volcanic-derived particles, T1 event-layers contain large non-weathered mica minerals (> 150 µm, Fig.

378 4b, c), which suggests a rapid terrigenous transfer from Blue Nile sources, potentially from the Dabus,

379 Didesa (Blue Nile Basin) and Gash (Atbara basin) rivers (Fig. 1b; Garzanti et al., 2015).

380 Owing to this converging array of evidence, we propose that T1 event-layers represent the successive

381 deposition of hyperpycnal flows overflowing on the right-hand levee of DSF6 (Fig. 7) during

382 exceptional and near-instantaneous flooding events, which rapidly transferred sediments eroded in

383 the Ethiopian Highlands to the western NDSF. This depositional model can even explain the difference

384 observed between T1α and T1β layers (Figs. 6, 7): during the low energy flood-induced phase, thin

385 hyperpycnal flows are constrained at the channel floor, producing a graded-suspended sedimentation

386 restricted to the levee crest (T1α). During the highest magnitude flood-induced flow phase, thick

387 hyperpycnal flows expand within the whole channel conduit and overflow the levee crest, generating

388 tractive processes that bring the coarsest grains over the levee area (T1β; Fig. 7).

389 In T1 event-layers, an increase of Mn/Al was systematically detected (Figs. 3, 4a, 6b). This enrichment

390 in Mn might be related to the delivery of oxygen to the bottom waters by hyperpycnal flows (oxic

391 freshwater front) that could be trapped in the porosity of the T1 beds. Mn would then be oxidized and

392 precipitated in the form of Mn-oxyhydroxides (e.g. Deflandre et al., 2002; Torres et al., 2014; Wilhelm

393 et al., 2016). Thus, we use here Mn/Al peaks as a marker of flood-induced deposit.

394 Regarding the T2 deposits, the presence of non-oriented organic matter, the more or less pronounced

395 Ti/K ratios and the Q90/Q10 peaks suggest a continental origin, but the systematic absence of Mn/Al

396 peaks (Figs. 3, 5a, 6b) also indicate a lack or lower amounts of fresh-water input. We propose that

397 normally-graded T2 layers result from low-energy turbidity currents generated by landslides triggered

398 at the Rosetta-Canyon head that reworked terrigenous and biogenic deposits from the outer

399 continental shelf (Fig. 5c). This hypothesis seems to be confirmed by Q90/Q50 values in T2, which are

400 consistent with uniform suspension processes resulting from a mixing of suspended material (Fig. 6b,

401 c). T2 beds will thereafter be excluded from the climatic interpretations.

402

403 ## 5.2 Coherence of Nile flood records over the upper slope of the Rosetta System

404 The frequency and the Nd isotopic signature of the hyperpycnal deposits (T1 event-layers recorded in

405 MD04-2726 core) and clastic-mud beds (recorded in MS27PT core; Fig. 1a; Sup. Mat. Fig. A.2, A.3) are

406 compared, with the aim of testing the coherence of these different Nile flood records over the Rosetta

407 upper slope. A similarity in elemental composition (increase of Ti/K and Mn/Al; Sup. Mat Fig. A.3) a

408 temporal coherence can be observed between the T1 event-layers and the clastic-mud deposits

409 recorded in core MS27PT (Fig. 8d, f; Revel et al. 2015). During strong floods, two types of processes

410 can be generated synchronously: a low-concentrated hypopycnal plume at the sea surface and a high-

411 concentrated hyperpycnal flow plunging at the bottom (Mulder et al., 2003; Mulder and Alexander,

412 2001). During exceptional Nile floods, we therefore suggest that the resultant hyperpycnal flows are

413 trapped within the Rosetta Canyon and channels and form T1 event-layers on levees (MD04-2726 core

414 site). Low-density hypopycnal plumes spread at the sea surface while their fine-grained suspended

415 particles are affected by decantation and convection processes along the water column, resulting in

416 the deposition of clastic-mud beds over more than 30 km on the continental slope (MS27PT and

417 PS3622-33core sites; Fig 7; Ducassou et al., 2009). The exceptional nature of the T1α and T1β floods,

418 occurring at an average of 1 to 7 events every 100 yr (Fig. 8b), suggests an intermittent high-energy

419 hydrological activation. As described in detail in paragraph 5.1.1, T1β could indicate higher-energy

420 floods than T1α event-layers.

421

422 5.3 Holocene hydro-climatic shifts over the Blue Nile basin

423 Our results document the frequency of exceptional (high-energy) Ethiopian Nile flood events during

424 the Early and Middle Holocene (~10.1 to ~7.3 ka BP; Fig. 9e). This multi-centennial paleo-flood

425 chronicle seems to be uniformly recorded in two piston-cores as hyperpycnal-flow deposits and

426 clastic-mud beds over the proximal Rosetta System (western NDSF; Fig. 8). We compared this flood

427 frequency record with the precipitation-induced runoff activity recorded at Lake Tana, as derived from

428 the Ti concentration profile (Figs. 1b, 9g; Marshall et al., 2011), and with the K and Ti events recorded

429 at Lake Dendi (Figs. 1b, 9f; Wagner et al., 2018) interpreted as an intense erosion and rainfall runoff at

430 the head of the Blue Nile Basin. Precise correlation between single runoff and flood events would be

431 hazardous because of the chronological uncertainty when comparing regional archives. However,

432 general trends of the selected proxies seem to be coherent at centennial-scale.

433 Fluctuations of radiogenic ƐNd values in both T1 layers and hemipelagic sediments in all cores from

434 the western NDSF (Fig. 9c, d, for MD04-2726 and MS27PT and Blanchet et al., 2014 for P362/2-33)

435 reflect changes in the proportion of eroded material from Ethiopian Traps. Similar source-to-sink

436 flood/runoff trends, combined with the high radiogenic εNd signature of T1 event-layers and clastic

437 mud deposits (Fig. 9c, 9d) demonstrate the capacity of the Nile drainage system to rapidly connect the

438 Ethiopian Traps source to its deep delta, and discredit the hypothesis of autogenic sediment transport

439 anomalies (non-linear geomorphic system; Jerolmack and Paola, 2010). Decrease in εNd values could

440 be explained by a higher contribution from the Equatorial-White Nile (African craton εNd = -30) or

441 from the lower-course White/Blue Nile sources (Saharan Metacraton imprint; Abdelsalam et al., 2002;

442 Grousset and Biscaye, 2005; Skonieczny et al., 2011). However, the Early to Mid-Holocene relative

443 elevated εNd values of the silt fraction show that the proportion of Ethiopian Traps material remained

444 high even during more arid periods (such as the 8.2 ka event; εNd = -4; Fig. 9c, d), hence clearly

445 suggesting persistent inputs from the Ethiopian Traps and/or on-going sediment transport via the Blue

446 Nile and the Sobat/Atbara rivers to the NDSF.

447 Based on correlation with other paleoclimatic and paleoenvironmental regional studies, the centennial

448 time resolution of flood-induced event-layers reveals three trends in Early to Mid-Holocene hydro-

449 climatic dynamics.

450 ### 5.3.1   *From 10 to 9 ka BP : a strong and stable hydro-climatic activity*

451 From 10.1 to 9 ka BP, more radiogenic εNd values of hemipelagic sediment (around -4.5), T1 event-

452 layers (-3 to -2; MD04-2726 core) and clastic mud beds from MS27PT core (-4 to -3, Fig. 9c, d)

453 demonstrate the dominant contribution of Ethiopian Traps material to the sedimentation in the

454 western NDSF. This is accompanied by high sedimentation rates in all three deltaic cores and therefore

455 suggests a large erosional activity in the Nile watershed (Fig. 1a, 8d, 8f). The paleo-flood frequency

456 reconstruction shows a strong increase of the Nile River's hydrological activity from 10.1 ka BP

457 onwards, which is in phase with maximal June insolation at 15°N (Fig. 9a). Exceptional Nile flood

458 events culminate at 9.5-9 ka BP with seven high-energy floods every 100 yr (Fig. 9e).

459 High precipitation-led runoff at Lake Dendi (Ti and K events, Fig. 9f, Wagner et al., 2018) and Lake Tana

460 (Ti content, Fig. 9g, Marshall et al., 2011), both located at the source of the Blue Nile, seem to occur

461   synchronously with intervals of the strongest Nile flood events (T1β layers; Fig. 9e). Additionally,

462   continental geomorphological data from the Blue and White Nile lower courses (Khartoum region;

463   Williams, 2009; Williams et al., 2015) seem coherent with our results: high energy exceptional T1β

464   event-layers are in phase (within age uncertainty) with enhanced Nile flood periods recorded until 9 ka

465   BP (Fig. 9h). This temporal coherency in runoff activity along the Nile River drainage basin suggests

466   strong erosion dynamics from the source to the sink of the fluvial system.

467   This strong erosional activity during the Early Holocene occurs during an interval of intense monsoonal

468   precipitations recorded from 10 ka BP onwards by low and constant δD_{wax} values at Lake Tana (Fig. 9b;

469   Costa et al., 2014), Lake Victoria (Berke et al., 2012) and by stable high water-levels of East African

470   lakes (Gasse, 2000; Junginger et al., 2014). We therefore propose the occurrence of enhanced

471   erosional activity within the whole drainage basin of the Nile River during the Early Holocene, largely

472   related to high and stable monsoonal rainfall on the Ethiopian Highlands.

473   *5.3.2. Stepwise Early Holocene hydro-climatic degradation from 9 ka BP*

474   From 9 ka BP onwards, ƐNd values of hemipelagic sediment and Ti layers from cores MD04-2726 and

475   MS27PT start to decrease following the progressive decrease in frequency of T1 event-layers and of

476   sedimentation rates in cores MS27PT and P362/2-33 (Fig. 8c-f). A lower frequency of T1α layers, rare

477   T1β event-layers and less radiogenic ƐNd values indicate that Nile hydrologic activity had reduced very

478   gradually from 9 until 7.8 ka BP, with an emphasis of reduction between 8.2 and 7.8 ka BP (Fig. 9c-e).

479   After a short-lived drop in flood frequency at 9 ka BP, the thickness of T1 event-layers and clastic-mud

480   beds slightly decrease, indicating a reduction of flood particle discharge and/or shorter-lasting floods

481   (Fig. 8a) while the higher Q90/Q50 ratio of T1 event-layers points to reduced flow energy (Fig. 8b). The

482   combination of reduced flood particle discharge, weakened transport energy and decreasing flood

483   frequency suggests a switch of the Nile River hydrological regime from episodic high-energy flood

484   discharge dynamics (between 10 and 9 ka BP) to low-energy and shorter-lasting flood discharge

485   dynamics (after 9 ka BP). This progressive shutdown of flood frequency and intensity, with more

486   negative εNd, culminates between 8.2 and 7.8 ka BP, suggesting an ~800 year-long stepwise Early

487   Holocene aridification interval (Fig. 9).

488   A distinct interruption of the Blue and White Nile flooding events was also recorded around 9 ka BP in

489   the Khartoum region (Fig. 9h; Williams, 2009), in phase with an interruption of rainfall-induced runoff

490   events at Lake Dendi (Fig. 9f; Wagner et al., 2018). Similarly, at Lake Tana a slight reduction in

491   precipitations is evidenced by δD_{wax} values around 9 ka BP (Fig. 9b; Costa et al., 2014) interpreted as

492   reflecting either a southward retreat of the monsoonal rain belt or an eastward shift of the Congo Air

493   Boundary. Changes in erosion and monsoonal dynamics as early as ~8.7 ka BP have already been

494   pointed out by previous studies (Blanchet et al., 2014; Ménot et al., 2020).

495   Subsequently, around 8.2 to 8 ka BP, a period of marked aridification was reported elsewhere in

496   North East Africa as a single event (Costa et al., 2014; Garcin et al., 2012; Gasse, 2000; Marshall et

497   al., 2011). A classical scenario suggests that high latitudes fully drove low-latitude hydrology at

498   millennial timescales (Collins et al., 2017). The onset of aridification in the Nile catchment would

499   then result from the release of freshwater in the North Atlantic during the 8.2 ka BP event,

500   leading to a slowdown of the Atlantic Meridional Overturning Circulation (AMOC) and/or a

501   decrease in arctic air temperatures which induces a decrease on the Tropical Easterly Jet (Collins

502   et al., 2017). These processes, together with a reduction in summer insolation, might have led to

503   drier conditions in tropical monsoonal areas.

504   However, this scenario does not account for a destabilization of the monsoonal system as early

505   as 9 ka BP, as seen in our record. The observed time lag between the beginning of the hydrologic

506   shift in East Africa at 9 ka BP and the North Atlantic 8.2 ka BP cooling event casts doubt on the

507   mechanisms linking high- and low-latitude hydrological changes (Collins et al., 2017; Mohtadi et al.,

508   2016). We propose here that an early shift of the main climatic boundaries above the Ethiopian

509   Highlands (Costa et al., 2014) linked with the gradual decrease in summer insolation might have

510   been sufficient to initiate a drier period in the tropics between 9 and 8 ka BP. Accordingly, recent

511   modelling experiments suggest that an obliquity-driven change in insolation gradient at low

512 latitudes might have directly enhanced monsoonal rainfall (Bosmans et al., 2015b; Mantsis et al.,

513 2014). Consequently, the insolation on the tropics could have had largely contributed in

514 generating air moisture masses over the oceans without the influence of the indirect energy-

515 balance inputs from high-latitude internal forcing and from North Atlantic ice-sea interactions

516 (Bosmans et al., 2015b, 2015a; Clement et al., 2015). Finally, has been even argued that the high-

517 latitude cooling events would be further enhanced by the decrease in African precipitation and

518 by Saharan aridification, which may have contributed to a tipping point behaviour between low

519 and high latitudes (Clement et al., 2001; Davies et al., 2014).

520

521 *5.3.3. Unstable and anomalous Nile hydrologic conditions from 7.8 ka BP*

522 The low ƐNd values observed from 7.8 ka BP in both T1 layers and hemipelagic sediments in all cores

523 from the western NDSF (Fig. 9c, d; for MD04-2726 and MS27PT and Blanchet et al., 2014 for P362/2-

524 33) indicate a lower contribution of Ethiopian Trap detrital particles suggesting a White Nile or lower-

525 course White and Blue Nile source contributions, characterized by a Saharan aeolian Metacraton

526 imprint (ƐNd from -10 to -14; Abdelsalam et al., 2002; Grousset and Biscaye, 2005; Scheuvens et al.,

527 2013).

528 After low flood activity around 8 ka BP, T1 event-layers resume from 7.8 ka BP onwards, with a

529 frequency of five event-layers/100 yr, thereby characterizing higher particle discharge (increase in T1

530 thickness; Fig. 8a), reduced flow energy (increase of Q90/Q50 ratio produced by Q50 drop) and a

531 reduction of Ethiopian Traps source inputs (lower ƐNd values; -4.5, Fig. 9c, d). Higher flood frequency

532 is associated with a high amount of T1β layers until 7.6 ka BP, and a reduction of flood frequency to

533 ca. 2.5 event-layers/100 yr is associated with a dominance of T1α layers (Fig. 9e). Contemporarily, leaf

534 wax deuterium isotopes at Lake Tana indicate lower precipitation over the Ethiopian Highlands, at the

535 source of the Blue Nile (Fig. 9b; Costa et al., 2011).

536 The occurrence of higher flood frequency and higher particle discharge during a lower rainfall period

537 shows a decoupling between erosive activity and climatic forcing, suggesting the development of an

538 "out of equilibrium" geomorphic system (i.e., the sedimentary input into the system is not equal to the

539 system output, Ahnert, 1994; Hoffmann, 2015). This anomaly could be explained by a process during

540 the entire 8.2-7.8 ka BP arid period whereby low precipitation favoured the fluvial riverbed

541 aggradation (i.e., storage effect; Phillips, 2003). The subsequent slight resumption of precipitation

542 post-7.8 ka BP (reduced δD_{WAX} at Lake Tana, Fig. 9b, f) led to a rapid erosion of the previously

543 deposited sediment with low radiogenic ƐNd values along the Nile course, producing a dense plume at

544 the river mouth and the large amount of T1 event-layers.

545 This is supported by other geomorphological data, which indicate the resumption of White Nile floods

546 in the Khartoum region from 7.8 ka BP, in phase with the numerous low radiogenic T1 event-layers

547 (Fig 9h, 9e; Williams, 2009; Williams et al., 2015). Following this scenario, drastic reduction in

548 vegetation cover over the Saharan Nile and the Sahelian belt (Hopcroft et al., 2017) during the 8.2 ka

549 BP event could have accentuated this process with an enhanced soil erosion.

550 Our results therefore show how at the end of abrupt arid climatic events, such as those occurring

551 around 8.2-7.8 ka BP, an "out of equilibrium" fluvial effect may occur, characterized by a

552 disproportionate sediment delivery to the continental margins and resulting in an autogenic

553 sedimentation process relatively decoupled from the climatic forcing.

554 From 7 ka BP, re-oxygenation of bottom waters in the Levantine area mark the end of S1 (De Lange et

555 al., 2008) and the end of the hyperpycnite-prone interval due to resumed bioturbation in MD04-2726

556 and MS27PT cores (Fig. 1d, 1e). The input of Blue Nile suspended material, as well as the flood energy,

557 decreased progressively until ~4 ka BP, thus preventing the formation of high dense plume capable to

558 induce hyperpycnal flows. Accordingly, the lowest ƐNd and Ti/K values were measured from

559 hemipelagic sediment (-6.5; Fig. 1b, c), corresponding to the ~4.2 ka BP drought event (Bini et al.,

560 2019).

6 - Conclusion

This study presents the first continuous reconstruction of exceptional Nile floods at centennial resolution from a well-preserved sedimentary interval from the Nile Deep-Sea Fan during the Early to the Middle Holocene. A multiproxy approach using sedimentological, geochemical (elemental contents and Nd isotopes) and microscopic methods have allowed us to identify instantaneous deposits (as hyperpycnites and clastic-mud beds) related to exceptional floods from the Blue Nile recorded in two cores from the upper slope of the Rosetta System. Similar trends between the occurrence of flood layers at centennial scale and changes in terrigenous input at Lake Tana (the source of the Blue Nile under direct influence of the African summer monsoon), as well their ƐNd signature, suggest their direct relationship to high-intensity and exceptional monsoon-related erosive and runoff events in the Ethiopian Highlands.

Our results enable us to draw some hydro-climatic inferences, in particular: a) the occurrence of recurrent (5 to 7/100 yr) high energy instantaneous floods between 10.1 and 9 ka BP during the height of the African Humid Period; b) a noticeable shift in the hydro-climatic regime around 9 ka BP characterized by a progressive reduction of Blue Nile input and by lower frequency and magnitude of floods until 8.2 ka BP; c) a low precipitation regime from 8.2 ka BP expressed in very low river runoff; d) the installation of an unstable and reduced Ethiopian-Nile hydrological regime from 7.8 ka BP where erosive activity and sediment transport is decoupled from climatic forcing, followed by a gradual reduction in precipitation intensity until ~4 ka BP.

In conclusion, we highlight the occurrence of a stepwise aridification process during the Early Holocene in the Blue Nile basin that questions the climatic linkages and feedbacks between low and high latitudes around the 8.2 ka BP North Atlantic cooling event. We also show how hyper-arid climatic episodes such as the 8.2 ka BP event might produce a destabilisation of the fluvial geomorphic system, inducing an anomaly of sediment transfer and the consequent autogenic sediment recording over the continental margin basins.

586

601

References

603   Abdelsalam, M.G., Liégeois, J.-P., Stern, R.J., 2002. The Saharan Metacraton. J. Afr. Earth Sci. 34, 119–
604   136. https://doi.org/10.1016/S0899-5362(02)00013-1
605   Ahnert, F., 1994. Equilibrium, scale and inheritance in geomorphology. Geomorphology 11, 125–140.
606   https://doi.org/10.1016/0169-555X(94)90077-9
607   Bastian, L., Revel, M., Bayon, G., Dufour, A., Vigier, N., 2017. Abrupt response of chemical weathering
608   to Late Quaternary hydroclimate changes in northeast Africa. Sci. Rep. 7, 44231.
609   https://doi.org/10.1038/srep44231
610   Bayon, G., German, C.R., Boella, R.M., Milton, J.A., Taylor, R.N., Nesbitt, R.W., 2002. An improved
611   method for extracting marine sediment fractions and its application to Sr and Nd isotopic
612   analysis. Chem. Geol. 187, 179–199. https://doi.org/10.1016/S0009-2541(01)00416-8
613   Be'eri-Shlevin, Y., Avigad, D., Gerdes, A., 2018. The White Nile as a source for Nile sediments:
614   Assessment using U-Pb geochronology of detrital rutile and monazite. J. Afr. Earth Sci. 140,
615   1–8. https://doi.org/10.1016/j.jafrearsci.2017.12.032
616   Berger, A., Loutre, M.F., 1991. Insolation values for the climate of the last 10 million years. Quat. Sci.
617   Rev. 10, 297–317. https://doi.org/10.1016/0277-3791(91)90033-Q

618   Berke, M.A., Johnson, T.C., Werne, J.P., Schouten, S., Sinninghe Damsté, J.S., 2012. A mid-Holocene
619   thermal maximum at the end of the African Humid Period. Earth Planet. Sci. Lett. 351–352,
620   95–104. https://doi.org/10.1016/j.epsl.2012.07.008
621   Bini, M., Zanchetta, G., Perşoiu, A., Cartier, R., Català, A., Cacho, I., Dean, J.R., Di Rita, F., Drysdale,
622   R.N., Finnè, M., Isola, I., Jalali, B., Lirer, F., Magri, D., Masi, A., Marks, L., Mercuri, A.M.,
623   Peyron, O., Sadori, L., Sicre, M.-A., Welc, F., Zielhofer, C., Brisset, E., 2019. The 4.2\,ka\,BP
624   Event in the Mediterranean region: an overview. Clim. Past 15, 555–577.
625   https://doi.org/10.5194/cp-15-555-2019
626   Blaauw, M., Christen, J.A., 2011. Flexible paleoclimate age-depth models using an autoregressive
627   gamma process. Bayesian Anal. 6, 457–474. https://doi.org/10.1214/ba/1339616472
628   Blanchet, C.L., 2019. A database of marine and terrestrial radiogenic Nd and Sr isotopes for tracing
629   earth-surface processes. Earth Syst. Sci. Data 11, 741–759. https://doi.org/10.5194/essd-11-
630   741-2019
631   Blanchet, C.L., Frank, M., Schouten, S., 2014. Asynchronous changes in vegetation, runoff and Erosion
632   in the Nile River watershed during the Holocene. PLoS ONE 9, 1–18.
633   https://doi.org/10.1371/journal.pone.0115958
634   Blanchet, C.L., Tjallingii, R., Frank, M., Lorenzen, J., Reitz, A., Brown, K., Feseker, T., Brückmann, W.,
635   2013. High- and low-latitude forcing of the Nile River regime during the Holocene inferred
636   from laminated sediments of the Nile deep-sea fan. Earth Planet. Sci. Lett. 364, 98–110.
637   https://doi.org/10.1016/j.epsl.2013.01.009
638   Blanchet, Frank, M., Schouten, S., 2014. Asynchronous Changes in Vegetation, Runoff and Erosion in
639   the Nile River Watershed during the Holocene. PLOS ONE 9, e115958.
640   https://doi.org/10.1371/journal.pone.0115958
641   Bosmans, J.H.C., Drijfhout, S.S., Tuenter, E., Hilgen, F.J., Lourens, L.J., 2015a. Response of the North
642   African summer monsoon to precession and obliquity forcings in the EC-Earth GCM. Clim.
643   Dyn. 44, 279–297. https://doi.org/10.1007/s00382-014-2260-z
644   Bosmans, J.H.C., Hilgen, F.J., Tuenter, E., Lourens, L.J., 2015b. Obliquity forcing of low-latitude
645   climate. Clim. Past 11, 1335–1346. https://doi.org/10.5194/cp-11-1335-2015
646   Bouvier, A., Vervoort, J.D., Patchett, P.J., 2008. The Lu–Hf and Sm–Nd isotopic composition of CHUR:
647   Constraints from unequilibrated chondrites and implications for the bulk composition of
648   terrestrial planets. Earth Planet. Sci. Lett. 273, 48–57.
649   https://doi.org/10.1016/j.epsl.2008.06.010
650   Bronk Ramsey, C.B., 2017. Methods for Summarizing Radiocarbon Datasets. Radiocarbon 59, 1809–
651   1833. https://doi.org/10.1017/RDC.2017.108
652   Chalié, F., Gasse, F., 2000. Late Glacial Holocene diatom record of water chemistry and lake level
653   change from the tropical East African Rift Lake Abiyata (Ethiopia). Palaeogeogr.
654   Palaeoclimatol. Palaeoecol. 187, 259–283.
655   Chauvel, C., Blichert-Toft, J., 2001. A hafnium isotope and trace element perspective on melting of
656   the depleted mantle. Earth Planet. Sci. Lett. 190, 137–151. https://doi.org/10.1016/S0012-
657   821X(01)00379-X
658   Clement, A., Bellomo, K., Murphy, L.N., Cane, M.A., Mauritsen, T., Radel, G., Stevens, B., 2015. The
659   Atlantic Multidecadal Oscillation without a role for ocean circulation. Science 350, 320–324.
660   https://doi.org/10.1126/science.aab3980
661   Clement, A.C., Cane, M.A., Seager, R., 2001. An Orbitally Driven Tropical Source for Abrupt Climate
662   Change. J. Clim. 14, 7.
663   Collins, J.A., Prange, M., Caley, T., Gimeno, L., Beckmann, B., Mulitza, S., Skonieczny, C., Roche, D.,
664   Schefuß, E., 2017. Rapid termination of the African Humid Period triggered by northern high-
665   latitude cooling. Nat. Commun. 8, 1372. https://doi.org/10.1038/s41467-017-01454-y
666   Collins, J.A., Schefuß, E., Heslop, D., Mulitza, S., Prange, M., Zabel, M., Tjallingii, R., Dokken, T.M.,
667   Huang, E., Mackensen, A., Schulz, M., Tian, J., Zarriess, M., Wefer, G., 2011. Interhemispheric
668   symmetry of the tropical African rainbelt over the past 23,000 years. Nat. Geosci. 4, 42–45.
669   https://doi.org/10.1038/ngeo1039

670   Costa, K., Russell, J., Konecky, B., Lamb, H., 2014. Isotopic reconstruction of the African Humid Period
671   and Congo Air Boundary migration at Lake Tana, Ethiopia. Quat. Sci. Rev. 83, 58–67.
672   https://doi.org/10.1016/j.quascirev.2013.10.031
673   Croudace, I.W., Rothwell, R.G. (Eds.), 2015. Micro-XRF Studies of Sediment Cores, Developments in
674   Paleoenvironmental Research. Springer Netherlands, Dordrecht.
675   https://doi.org/10.1007/978-94-017-9849-5
676   Davies, F.J., Renssen, H., Blaschek, M., Muschitiello, F., 2014. The impact of Sahara desertification on
677   Arctic cooling during the Holocene. Clim. Past Discuss. 10, 1653–1673.
678   https://doi.org/10.5194/cpd-10-1653-2014
679   De Lange, G.J., Thomson, J., Reitz, A., Slomp, C.P., Speranza Principato, M., Erba, E., Corselli, C., 2008.
680   Synchronous basin-wide formation and redox-controlled preservation of a Mediterranean
681   sapropel. Nat. Geosci. 1, 606–610. https://doi.org/10.1038/ngeo283
682   Deflandre, B., Mucci, A., Gagné, J.-P., Guignard, C., Sundby, B. jørn, 2002. Early diagenetic processes
683   in coastal marine sediments disturbed by a catastrophic sedimentation event. Geochim.
684   Cosmochim. Acta 66, 2547–2558. https://doi.org/10.1016/S0016-7037(02)00861-X
685   deMenocal, P., Ortiz, J., Guilderson, T., Adkins, J., Sarnthein, M., Baker, L., Yarusinsky, M., 2000.
686   Abrupt onset and termination of the African Humid Period: rapid climate responses to
687   gradual insolation forcing. Quat. Sci. Rev. 19, 347–361.
688   Dewar, G., Reimer, P.J., Sealy, J., Woodborne, S., 2012. Late-Holocene marine radiocarbon reservoir
689   correction (ΔR) for the west coast of South Africa. The Holocene 22, 1481–1489.
690   https://doi.org/10.1177/0959683612449755
691   Ducassou, E., Capotondi, L., Murat, A., Bernasconi, S.M., Mulder, T., Gonthier, E., Migeon, S., Duprat,
692   J., Giraudeau, J., Mascle, J., 2007. Multiproxy Late Quaternary stratigraphy of the Nile deep-
693   sea turbidite system — Towards a chronology of deep-sea terrigeneous systems. Sediment.
694   Geol. 200, 1–13. https://doi.org/10.1016/j.sedgeo.2007.01.023
695   Ducassou, E., Migeon, S., Mulder, T., Murat, A., Capotondi, L., Bernasconi, S.M., Mascle, J., 2009.
696   Evolution of the Nile deep-sea turbidite system during the Late Quaternary: influence of
697   climate change on fan sedimentation. Sedimentology 56, 2061–2090.
698   https://doi.org/10.1111/j.1365-3091.2009.01070.x
699   Ducassou, E., Mulder, T., Migeon, S., Gonthier, E., Murat, A., Revel, M., Capotondi, L., Bernasconi,
700   S.M., Mascle, J., Zaragosi, S., 2008. Nile floods recorded in deep Mediterranean sediments.
701   Quat. Res. 70, 382–391. https://doi.org/10.1016/j.yqres.2008.02.011
702   Foerster, V., Junginger, A., Langkamp, O., Gebru, T., Asrat, A., Umer, M., Lamb, H.F., Wennrich, V.,
703   Rethemeyer, J., Nowaczyk, N., Trauth, M.H., Schaebitz, F., 2012. Climatic change recorded in
704   the sediments of the Chew Bahir basin, southern Ethiopia, during the last 45,000 years. Quat.
705   Int. 274, 25–37. https://doi.org/10.1016/j.quaint.2012.06.028
706   Folk, R.L., Ward, W.C., 1957. Brazos River Bar: A Study in the Significance of Grain Size Parameters. J.
707   Sediment. Petrol. 27, 3–26.
708   Garcin, Y., Melnick, D., Strecker, M.R., Olago, D., Tiercelin, J.-J., 2012. East African mid-Holocene wet–
709   dry transition recorded in palaeo-shorelines of Lake Turkana, northern Kenya Rift. Earth
710   Planet. Sci. Lett. 331–332, 322–334. https://doi.org/10.1016/j.epsl.2012.03.016
711   Garzanti, E., Andò, S., Padoan, M., Vezzoli, G., El Kammar, A., 2015. The modern Nile sediment
712   system: Processes and products. Quat. Sci. Rev. 130, 9–56.
713   https://doi.org/10.1016/j.quascirev.2015.07.011
714   Gasse, F., 2000. Hydrological changes in the African tropiccs since the Last Glacial Maximum. Quat.
715   Sci. Rev. 19, 189–211.
716   Grousset, F.E., Biscaye, P.E., 2005. Tracing dust sources and transport patterns using Sr, Nd and Pb
717   isotopes. Chem. Geol. 222, 149–167. https://doi.org/10.1016/j.chemgeo.2005.05.006
718   Hoffmann, T., 2015. Sediment residence time and connectivity in non-equilibrium and transient
719   geomorphic systems. Earth-Sci. Rev. 150, 609–627.
720   https://doi.org/10.1016/j.earscirev.2015.07.008

721 Hopcroft, P.O., Valdes, P.J., Harper, A.B., Beerling, D.J., 2017. Multi vegetation model evaluation of
722   the Green Sahara climate regime: RAINFALL SUPPORTING A GREEN SAHARA. Geophys. Res.
723   Lett. 44, 6804–6813. https://doi.org/10.1002/2017GL073740
724 Jerolmack, D.J., Paola, C., 2010. Shredding of environmental signals by sediment transport: SIGNAL
725   SHREDDING. Geophys. Res. Lett. 37, n/a-n/a. https://doi.org/10.1029/2010GL044638
726 Junginger, A., Roller, S., Olaka, L.A., Trauth, M.H., 2014. The effects of solar irradiation changes on
727   the migration of the Congo Air Boundary and water levels of paleo-Lake Suguta, Northern
728   Kenya Rift, during the African Humid Period (15–5ka BP). Palaeogeogr. Palaeoclimatol.
729   Palaeoecol. 396, 1–16. https://doi.org/10.1016/j.palaeo.2013.12.007
730 Krom, M.D., Stanley, J.D., Cliff, R.A., Woodward, J.C., 2002. Nile River sediment fluctuations over the
731   past 7000 yr and their key role in sapropel development 5.
732 Mantsis, D.F., Lintner, B.R., Broccoli, A.J., Erb, M.P., Clement, A.C., Park, H.-S., 2014. The Response of
733   Large-Scale Circulation to Obliquity-Induced Changes in Meridional Heating Gradients. J.
734   Clim. 27, 5504–5516. https://doi.org/10.1175/JCLI-D-13-00526.1
735 Marshall, M.H., Lamb, H.F., Huws, D., Davies, S.J., Bates, R., Bloemendal, J., Boyle, J., Leng, M.J.,
736   Umer, M., Bryant, C., 2011. Late Pleistocene and Holocene drought events at Lake Tana, the
737   source of the Blue Nile. Glob. Planet. Change 78, 147–161.
738   https://doi.org/10.1016/j.gloplacha.2011.06.004
739 Mascle, J., Sardou, O., Loncke, L., Migeon, S., Caméra, L., Gaullier, V., 2006. Morphostructure of the
740   Egyptian Continental Margin: Insights from Swath Bathymetry Surveys. Mar. Geophys. Res.
741   27, 49–59. https://doi.org/10.1007/s11001-005-1559-x
742 Ménot, G., Pivot, S., Bouloubassi, I., Davtian, N., Hennekam, R., Bosch, D., Ducassou, E., Bard, E.,
743   Migeon, S., Revel, M., 2020. Timing and stepwise transitions of the African Humid Period
744   from geochemical proxies in the Nile deep-sea fan sediments. Quat. Sci. Rev. 228, 106071.
745   https://doi.org/10.1016/j.quascirev.2019.106071
746 Migeon, S., Ducassou, E., Le Gonidec, Y., Rouillard, P., Mascle, J., Revel-Rolland, M., 2010. Lobe
747   construction and sand/mud segregation by turbidity currents and debris flows on the
748   western Nile deep-sea fan (Eastern Mediterranean). Sediment. Geol. 229, 124–143.
749   https://doi.org/10.1016/j.sedgeo.2010.02.011
750 Migeon, S., Savoye, B., Zanella, E., Mulder, T., 2001. Detailed seismic-reˉection and sedimentary
751   study of turbidite sediment waves on the Var Sedimentary Ridge (SE France): signi®cance for
752   sediment transport and deposition and for the mechanisms of sediment-wave construction.
753   Mar. Pet. Geol. 30.
754 Mohtadi, M., Prange, M., Steinke, S., 2016. Palaeoclimatic insights into forcing and response of
755   monsoon rainfall. Nature 533, 191–199. https://doi.org/10.1038/nature17450
756 Mulder, T., Alexander, J., 2001. The physical character of subaqueous sedimentary density ˉows and
757   their deposits 31.
758 Mulder, T., Migeon, S., Savoye, B., Faugères, J.-C., 2001. Inversely graded turbidite sequences in the
759   deep Mediterranean: a record of deposits from flood-generated turbidity currents? Geo-Mar.
760   Lett. 21, 86–93. https://doi.org/10.1007/s003670100071
761 Mulder, T., Syvitski, J.P.M., Migeon, S., Faugères, J.-C., Savoye, B., 2003. Marine hyperpycnal flows:
762   initiation, behavior and related deposits. A review. Mar. Pet. Geol. 20, 861–882.
763   https://doi.org/10.1016/j.marpetgeo.2003.01.003
764 Mulitza, S., Prange, M., Stuut, J.-B., Zabel, M., von Dobeneck, T., Itambi, A.C., Nizou, J., Schulz, M.,
765   Wefer, G., 2008. Sahel megadroughts triggered by glacial slowdowns of Atlantic meridional
766   overturning: SAHEL DROUGHT AND ATLANTIC OVERTURNING. Paleoceanography 23, n/a-n/a.
767   https://doi.org/10.1029/2008PA001637
768 Padoan, M., Garzanti, E., Harlavan, Y., Villa, I.M., 2011. Tracing Nile sediment sources by Sr and Nd
769   isotope signatures (Uganda, Ethiopia, Sudan). Geochim. Cosmochim. Acta 75, 3627–3644.
770   https://doi.org/10.1016/j.gca.2011.03.042

771 Parsons, J.D., Bush, J.W.M., Syvitski, J.P.M., 2001. Hyperpycnal plume formation from riverine
772   outflows with small sediment concentrations. Sedimentology 48, 465–478.
773   https://doi.org/10.1046/j.1365-3091.2001.00384.x
774 Phillips, J.D., 2003. Sources of nonlinearity and complexity in geomorphic systems. Prog. Phys. Geogr.
775   Earth Environ. 27, 1–23. https://doi.org/10.1191/0309133303pp340ra
776 Prospero, J.M., Ginoux, P., Torres, O., Nicholson, S.E., Gill, T.E., 2002. Environmental characterization
777   of global sources of atmospheric soil dust identified with the NIMBUS 7 Total Ozone Mapping
778   Spectrometer (TOMS) absorbing aerosol product. Rev. Geophys. 40, 1–31.
779   https://doi.org/10.1029/2000RG000095
780 Reimer, P.J., Bard, E., Bayliss, A., Beck, J.W., Blackwell, P.G., Ramsey, C.B., Buck, C.E., Cheng, H.,
781   Edwards, R.L., Friedrich, M., Grootes, P.M., Guilderson, T.P., Haflidason, H., Hajdas, I., Hatté,
782   C., Heaton, T.J., Hoffmann, D.L., Hogg, A.G., Hughen, K.A., Kaiser, K.F., Kromer, B., Manning,
783   S.W., Niu, M., Reimer, R.W., Richards, D.A., Scott, E.M., Southon, J.R., Staff, R.A., Turney,
784   C.S.M., van der Plicht, J., 2013. IntCal13 and Marine13 Radiocarbon Age Calibration Curves 0–
785   50,000 Years cal BP. Radiocarbon 55, 1869–1887.
786   https://doi.org/10.2458/azu_js_rc.55.16947
787 Reimer, P.J., McCormac, F.G., Moore, J., McCormick, F., Murray, E.V., 2002. Marine radiocarbon
788   reservoir corrections for the midto late Holocene in the eastern subpolar North Atlantic. The
789   Holocene 12, 129–135. https://doi.org/10.1191/0959683602hl528rp
790 Reimer, R.W., Reimer, P.J., 2017. An Online Application for ΔR Calculation. Radiocarbon 59, 1623–
791   1627. https://doi.org/10.1017/RDC.2016.117
792 Revel, M., Ducassou, E., Grousset, F.E., Bernasconi, S.M., Migeon, S., Revillon, S., Mascle, J., Murat,
793   A., Zaragosi, S., Bosch, D., 2010. 100,000 Years of African monsoon variability recorded in
794   sediments of the Nile margin. Quat. Sci. Rev. 29, 1342–1362.
795   https://doi.org/10.1016/j.quascirev.2010.02.006
796 Revel, M., Ducassou, E., Skonieczny, C., Colin, C., Bastian, L., Bosch, D., Migeon, S., Mascle, J., 2015.
797   20,000 years of Nile River dynamics and environmental changes in the Nile catchment area
798   as inferred from Nile upper continental slope sediments. Quat. Sci. Rev. 130.
799   https://doi.org/10.1016/j.quascirev.2015.10.030
800 Revel, Marie, Ducassou, E., Skonieczny, C., Colin, C., Bastian, L., Bosch, D., Migeon, S., Mascle, J.,
801   2015. 20,000 years of Nile River dynamics and environmental changes in the Nile catchment
802   area as inferred from Nile upper continental slope sediments. Quat. Hist. River Nile 130, 200–
803   221. https://doi.org/10.1016/j.quascirev.2015.10.030
804 Rohling, E.J., Pälike, H., 2005. Centennial-scale climate cooling with a sudden cold event around 8,200
805   years ago. Nature 434, 975–979. https://doi.org/10.1038/nature03421
806 Rossignol-Strick, M., Nesteroff, W., Olive, P., Vergnaud-Grazzini, C., 1982. After the deluge:
807   Mediterranean stagnation and sapropel formation. Nature 295, 105–110.
808   https://doi.org/10.1038/295105a0
809 Santisteban, J.I., Mediavilla, R., López-Pamo, E., Dabrio, C.J., Blanca Ruiz Zapata, M., José Gil García,
810   M., Castaño, S., Martínez-Alfaro, P.E., 2004. Loss on ignition: a qualitative or quantitative
811   method for organic matter and carbonate mineral content in sediments? J. Paleolimnol. 32,
812   287–299. https://doi.org/10.1023/B:JOPL.0000042999.30131.5b
813 Schefuß, E., Eglinton, T.I., Spencer-Jones, C.L., Rullkötter, J., De Pol-Holz, R., Talbot, H.M., Grootes,
814   P.M., Schneider, R.R., 2016. Hydrologic control of carbon cycling and aged carbon discharge
815   in the Congo River basin. Nat. Geosci. 9, 687–690. https://doi.org/10.1038/ngeo2778
816 Scheuvens, D., Schütz, L., Kandler, K., Ebert, M., Weinbruch, S., 2013. Bulk composition of northern
817   African dust and its source sediments — A compilation. Earth-Sci. Rev. 116, 170–194.
818   https://doi.org/10.1016/j.earscirev.2012.08.005
819 Shanahan, T.M., McKay, N.P., Hughen, K.A., Overpeck, J.T., Otto-Bliesner, B., Heil, C.W., King, J.,
820   Scholz, C.A., Peck, J., 2015. The time-transgressive termination of the African Humid Period.
821   Nat. Geosci. 8, 140–144. https://doi.org/10.1038/ngeo2329

822 Siani, G., 2001. Mediterranean Sea Surface Radiocarbon Reservoir Age Changes Since the Last Glacial
823   Maximum. Science 294, 1917–1920. https://doi.org/10.1126/science.1063649
824 Skonieczny, C., Bory, A., Bout-Roumazeilles, V., Abouchami, W., Galer, S.J.G., Crosta, X., Stuut, J.-B.,
825   Meyer, I., Chiapello, I., Podvin, T., Chatenet, B., Diallo, A., Ndiaye, T., 2011. The 7–13 March
826   2006 major Saharan outbreak: Multiproxy characterization of mineral dust deposited on the
827   West African margin. J. Geophys. Res. 116, D18210. https://doi.org/10.1029/2011JD016173
828 Skonieczny, C., McGee, D., Winckler, G., Bory, A., Bradtmiller, L.I., Kinsley, C.W., Polissar, P.J., De Pol-
829   Holz, R., Rossignol, L., Malaizé, B., 2019. Monsoon-driven Saharan dust variability over the
830   past 240,000 years. Sci. Adv. 5, eaav1887. https://doi.org/10.1126/sciadv.aav1887
831 Skonieczny, C., Paillou, P., Bory, A., Bayon, G., Biscara, L., Crosta, X., Eynaud, F., Malaizé, B., Revel, M.,
832   Aleman, N., Barusseau, J.-P., Vernet, R., Lopez, S., Grousset, F., 2015. African humid periods
833   triggered the reactivation of a large river system in Western Sahara. Nat. Commun. 6, 8751.
834   https://doi.org/10.1038/ncomms9751
835 Thomson, J., Mercone, D., De Lange, G.J., Van Santvoort, P.J.M., 1999. Review of recent advances in
836   the interpretation of eastern Mediterranean sapropel S1 from geochemical evidence. Mar.
837   Geol. 153, 77–89. https://doi.org/10.1016/S0025-3227(98)00089-9
838 Tierney, J.E., deMenocal, P., 2013. Abrupt Shifts in Horn of Africa Hydroclimate Since the Last Glacial
839   Maximum. Science 342, 843–846. https://doi.org/10.1126/science.1244809
840 Torres, N.T., Och, L.M., Hauser, P.C., Furrer, G., Brandl, H., Vologina, E., Sturm, M., Bürgmann, H.,
841   Müller, B., 2014. Early diagenetic processes generate iron and manganese oxide layers in the
842   sediments of Lake Baikal, Siberia. Env. Sci Process. Impacts 16, 879–889.
843   https://doi.org/10.1039/C3EM00676J
844 Verschuren, D., Sinninghe Damsté, J.S., Moernaut, J., Kristen, I., Blaauw, M., Fagot, M., Haug, G.H.,
845   van Geel, B., De Batist, M., Barker, P., Vuille, M., Conley, D.J., Olago, D.O., Milne, I., Plessen,
846   B., Eggermont, H., Wolff, C., Hurrell, E., Ossebaar, J., Lyaruu, A., van der Plicht, J., Cumming,
847   B.F., Brauer, A., Rucina, S.M., Russell, J.M., Keppens, E., Hus, J., Bradley, R.S., Leng, M.,
848   Mingram, J., Nowaczyk, N.R., 2009. Half-precessional dynamics of monsoon rainfall near the
849   East African Equator. Nature 462, 637–641. https://doi.org/10.1038/nature08520
850 Viste, E., Sorteberg, A., 2013. Moisture transport into the Ethiopian highlands: MOISTURE
851   TRANSPORT INTO THE ETHIOPIAN HIGHLANDS. Int. J. Climatol. 33, 249–263.
852   https://doi.org/10.1002/joc.3409
853 Vos, K., Vandenberghe, N., Elsen, J., 2014. Surface textural analysis of quartz grains by scanning
854   electron microscopy (SEM): From sample preparation to environmental interpretation. Earth-
855   Sci. Rev. 128, 93–104. https://doi.org/10.1016/j.earscirev.2013.10.013
856 Wagner, B., Wennrich, V., Viehberg, F., Junginger, A., Kolvenbach, A., Rethemeyer, J., Schaebitz, F.,
857   Schmiedl, G., 2018. Holocene rainfall runoff in the central Ethiopian highlands and evolution
858   of the River Nile drainage system as revealed from a sediment record from Lake Dendi. Glob.
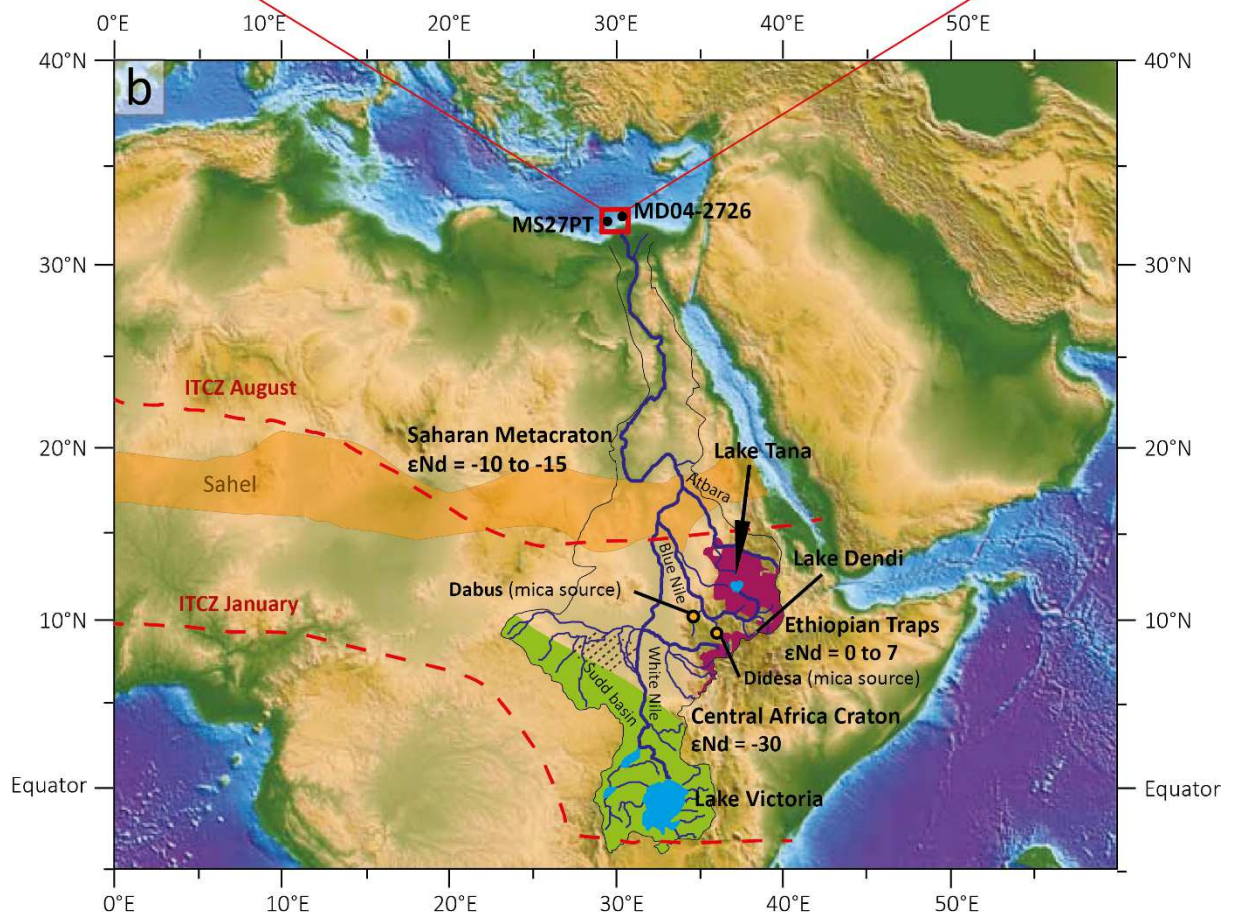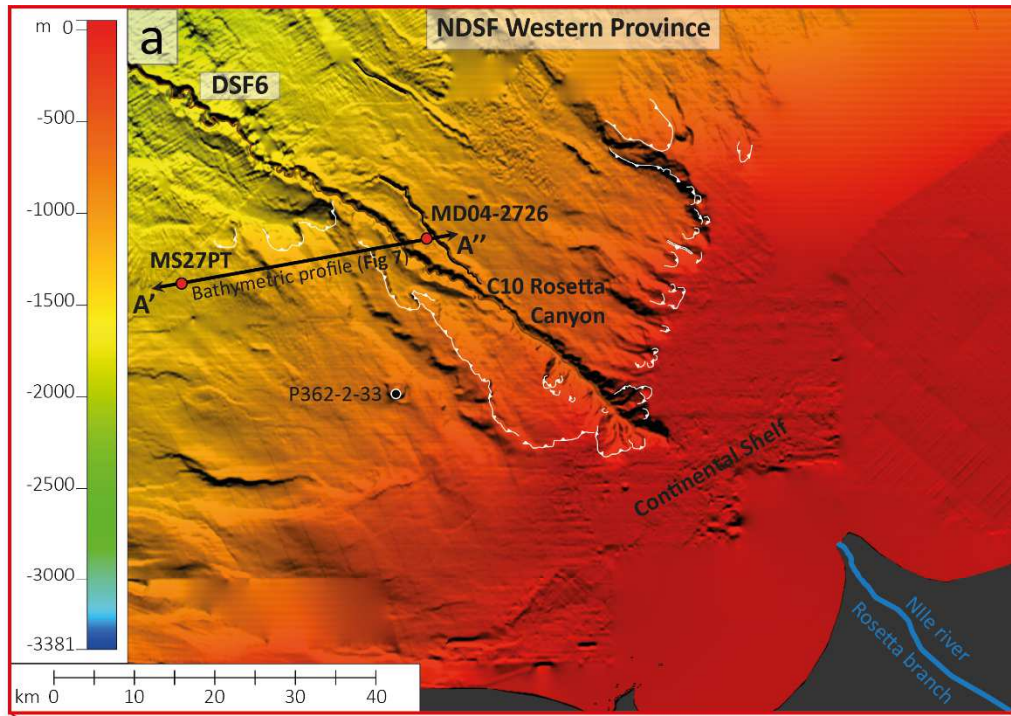859   Planet. Change 163, 29–43. https://doi.org/10.1016/j.gloplacha.2018.02.003
860 Weldeab, S., Emeis, K.-C., Hemleben, C., Vennemann, T.W., Schulz, H., 2002. Sr and Nd isotope
861   composition of Late Pleistocene sapropels and nonsapropelic sediments from the Eastern
862   Mediterranean Sea: implications for detrital influx and climatic conditions in the source
863   areas. Geochim. Cosmochim. Acta 66, 3585–3598. https://doi.org/10.1016/S0016-
864   7037(02)00954-7
865 Weltje, G.J., Tjallingii, R., 2008. Calibration of XRF core scanners for quantitative geochemical logging
866   of sediment cores: Theory and application. Earth Planet. Sci. Lett. 274, 423–438.
867   https://doi.org/10.1016/j.epsl.2008.07.054
868 Wilhelm, B., Vogel, H., Crouzet, C., Etienne, D., Anselmetti, F.S., 2016. Frequency and intensity of
869   palaeofloods at the interface of Atlantic and Mediterranean climate domains. Clim. Past 12,
870   299–316. https://doi.org/10.5194/cp-12-299-2016
871 Williams, M.A.J., 2009. Late Pleistocene and Holocene environments in the Nile basin. Glob. Planet.
872   Change 69, 1–15. https://doi.org/10.1016/j.gloplacha.2009.07.005

873   Williams, M.A.J., Usai, D., Salvatori, S., Williams, F.M., Zerboni, A., Maritan, L., Linseele, V., 2015. Late
874   Quaternary environments and prehistoric occupation in the lower White Nile valley, central
875   Sudan. Quat. Sci. Rev. 130, 72–88. https://doi.org/10.1016/j.quascirev.2015.03.007
876   Zirks, E., Krom, M.D., Zhu, D., Schmiedl, G., Goodman-Tchernov, B.N., 2019. Evidence for the
877   Presence of Oxygen-Depleted Sapropel Intermediate Water across the Eastern
878   Mediterranean during Sapropel S1. ACS Earth Space Chem. 3, 2287–2297.
879   https://doi.org/10.1021/acsearthspacechem.9b00128
880

Figure a — NDSF Western Province

Labels in panel a: DSF6, MD04-2726, A'', MS27PT, A', Bathymetric profile (Fig 7), C10 Rosetta Canyon, P362-2-33, Continental Shelf, Nile river, Rosetta branch

Labels in panel b: MS27PT, MD04-2726, ITCZ August, Sahel, Saharan Metacraton εNd = -10 to -15, ITCZ January, Lake Tana, Atbara, Lake Dendi, Dabus (mica source), Blue Nile, Ethiopian Traps εNd = 0 to 7, Didesa (mica source), Sudd basin, White Nile, Central Africa Craton εNd = -30, Lake Victoria

881

882 **Fig 1: a**) Bathymetric map of the Western Nile Deep Sae Fan (NDSF; proximal Rosetta Upper slope, C10

883 Rosetta canyon, DSF6) showing the locations of the studied cores MD04-2726 (31°51.00' N, 29°47.49'

884 E, 1058 m water depth) and MS27PT (N31_47.90'; E29_27.700, 1389 m water depth; red dots), the

885 bathymetric profile presented in Fig 7, and the P362-2-33 core (Blanchet et al., 2013, black dot). **b**)

886 Hydrological context of North Africa and the present-day active Nile watershed (modified from

887 Skonieczny et al., 2015). Three main sources of suspended sediment load are identified in the Nile

888 Deep-Sea Fan: the basaltic rocks (purple) of the Ethiopian Traps (Highlands), which are drained by the

889 Blue Nile, the Atbara and Sobat rivers located at tropical latitude (around 5 to 15°N); the Precambrian

890 metamorphic rocks (green) of the Central African Craton located in the equatorial latitude of Lakes

891 Albert and Victoria in the Ugandan headwaters region of the White Nile; the Saharan Metacraton

892 (Abdelsalam et al., 2002) which produce aeolian dust representing the source region of most deflation

893 documented by (Prospero et al., 2002; Scheuvens et al., 2013). The outcrops of the Ethiopian Traps,

894 Precambrian Craton and Saharan Metacraton provide sediments characterized by εNd values of > 0, >

895 -30 and from -10 to -14 respectively (Garzanti et al., 2015; Grousset and Biscaye, 2005; Skonieczny et

896 al., 2011). The seasonal positions of the Intertropical Convergence Zone (ITCZ; red dotted line, Viste

897 and Sorteberg, 2013) as well as of the Sahel zone (orange area) are shown, as well as the Nile

898 catchment mica sources (Dabus and Diesda rivers, orange dots; after Garzanti et al., 2015). **Fig 1: a**)

899 Bathymetric map of the Nile Deep Delta Western margin (proximal Rosetta Upper slope, C10 Rosetta

900 canyon, DSF6) showing the locations of the studied cores MD04-2726 (31°51.00' N, 29°47.49' E, 1058

901 m water depth) and MS27PT (N31_47.90'; E29_27.700, 1389 m water depth; red dots), the

902 bathymetric profile presented in Fig 7, and the P362-2-33 core (Blanchet et al., 2013, black dot). **b**)

903 Hydrological context of North Africa and the present-day active Nile watershed (modified from

904 Skonieczny et al., 2015).Three main sources of suspended sediment load are identified in the Nile

905 Deep-Sea Fan: the basaltic rocks (purple) of the Ethiopian Traps (Highlands), which are drained by the

906 Blue Nile, the Atbara and Sobat rivers located in tropical latitude (around 5 to 15°N); the Precambrian

907 metamorphic rocks (green) of the Central African Craton located in the equatorial latitude of the lakes

Lab. Code	Depth (cm)	Material	Radiocarbon age (^{14}C yr BP± 1σ)	Carbon content (mg)	Reservoir correction (yr)	Cal Curve	Calibrated age (cal yr BP ± 2σ)	Bacon median age (cal. yr BP ± 2σ)

908 Albert and Victoria in the Ugandan headwaters region of the White Nile; the Saharan Metacraton

909 (Abdelsalam et al., 2002) which produce aeolian dusts representing the source region of most

910 deflation documented by (Prospero et al., 2002; Scheuvens et al., 2013). The outcrops of the Ethiopian

911 Traps, Precambrian Craton and Saharan Metacraton provide sediments characterised by εNd values of

912 > 0, > -30 and from -10 to -14 respectively (Garzanti et al., 2015; Grousset and Biscaye, 2005;

913 Skonieczny et al., 2011). The seasonal positions of the Intertropical Convergence Zone (ITCZ; red

914 dotted line, Viste and Sorteberg, 2013) as well as of the Sahel zone (orange area) are shown, as well as

915 the Nile catchment mica sources (Dabus and Diesda rivers, orange dots; after Garzanti et al., 2015).

916

917

918

919

920

921

922

923

924

925

926

SacA16520	2	G. ruber alba	970	± 30	0.8	0	Marine13	564 ± 32	601 ± 71
SacA53733 *	5	Planktonic for.	1115	± 30	0.44	0	Marine13	670 ± 28	662 ± 62
SacA53734*	9	Planktonic for.	1315	± 30	0.59	0	Marine13	858 ± 41	829 ± 100
SacA53735 *	13	Planktonic for.	1595	± 30	0.94	0	Marine13	1162 ± 46	1094 ± 177
SacA53736 *	17	Planktonic for.	1865	± 30	0.72	0	Marine13	1409 ± 47	1392 ± 204
SacA16521	20	G. ruber alba	2105	± 30	1.2	0	Marine13	1684 ± 52	1568 ± 227
SacA53737 *	25	Planktonic for.	2425	± 35	1.02	0	Marine13	2062 ± 55	2136 ± 152
SacA53738 *	27	Planktonic for.	2855	± 30	1.03	0	Marine13	2633 ± 61	2435 ± 312
SacA35503*	31	G. ruber alba	3220	± 30	1.28	0	Marine13	3028 ± 56	2986 ± 158
SacA22281	35	G. ruber alba	3365	± 30	0.96	0	Marine13	3229 ± 52	3226 ± 98
SacA53739*	39	Planktonic for.	3505	± 30	0.95	0	Marine13	3398 ± 40	3360 ± 89
SacA22280	41	G. ruber alba	3525	± 30	0.99	0	Marine13	3409 ± 41	3425 ± 99
SacA53740 *	45	Planktonic for.	3735	± 30	1.04	0	Marine13	3657 ± 52	3582 ± 139
SacA53741 *	49	Planktonic for.	3915	± 30	0.78	0	Marine13	3894 ± 50	3877 ± 218
SacA22279	55	G. ruber alba	4590	± 30	0.69	0	Marine13	4813 ± 41	4651 ± 318
SacA53742 *	61	Planktonic for.	4870	± 30	0.64	0	Marine13	5186 ± 66	5260 ± 236
SacA16523	70.5	G. ruber alba	5465	± 30	0.26	0	Marine13	5845 ± 47	5801 ± 154
SacA35504 *	108.5	G. ruber alba	6700	± 30	0.61	0	Marine13	7229 ± 37	7100 ± 158
SacA16524	128	G. ruber alba	7085	± 35	0.3	0	Marine13	7564 ± 38	7233 ± 123
SacA35505	142	Bulk for.	6790	± 30	1.11	0	Marine13	7317 ± 40	7300 ± 87
SacA38937	191	Vegetal macrorest	8160	± 30	0.751	1854	IntCal13	7227 ± 35	7445 ± 52
Poz-108962 *	228	Bulk OC	8670	± 40	0.873	1854	IntCal13	7649 ± 33	7629 ± 103
Poz-108961 *	365	Bulk OC	9020	± 50	0.477	1854	IntCal13	7989 ± 52	8130 ± 151
Poz-108959 *	477	Bulk OC	10210	± 50	0.973	1854	IntCal13	9380 ± 66	8707 ± 152
SacA53743 *	499	Planktonic for.	6395	± 30	0.46	0	Marine13	6870 ± 49	8804 ± 148
Poz-108958 *	551	Bulk OC	9720	± 50	0.759	1854	IntCal13	8713 ± 104	9070 ± 111
Poz-105356 *	653	Bulk OC	9890	± 50	2.391	1854	IntCal13	8897 ± 94	9743 ± 182
SacA16525	658	G. ruber alba	9045	± 45	0.6	0	Marine13	9736 ± 90	9785 ± 159
Poz-105342 *	658.5	Bulk OC	10620	± 50	2.014	1854	IntCal13	9781 ± 117	9793 ± 160
Poz-105341 *	728	Bulk OC	10930	± 60	2.891	1854	IntCal13	10248 ± 74	10353 ± 153

927

Tab 1: Calibration of new and previous ages on MD04-2726 core, and result from age model building using the Bacon software (v3.6.3, Blaauw and Christen, 2011) based on Marine13 and IntCal13 calibration curves (Reimer et al. 2013). Bulk OC = Bulk Organic Carbon; * = new ages (this study).

931

932

933
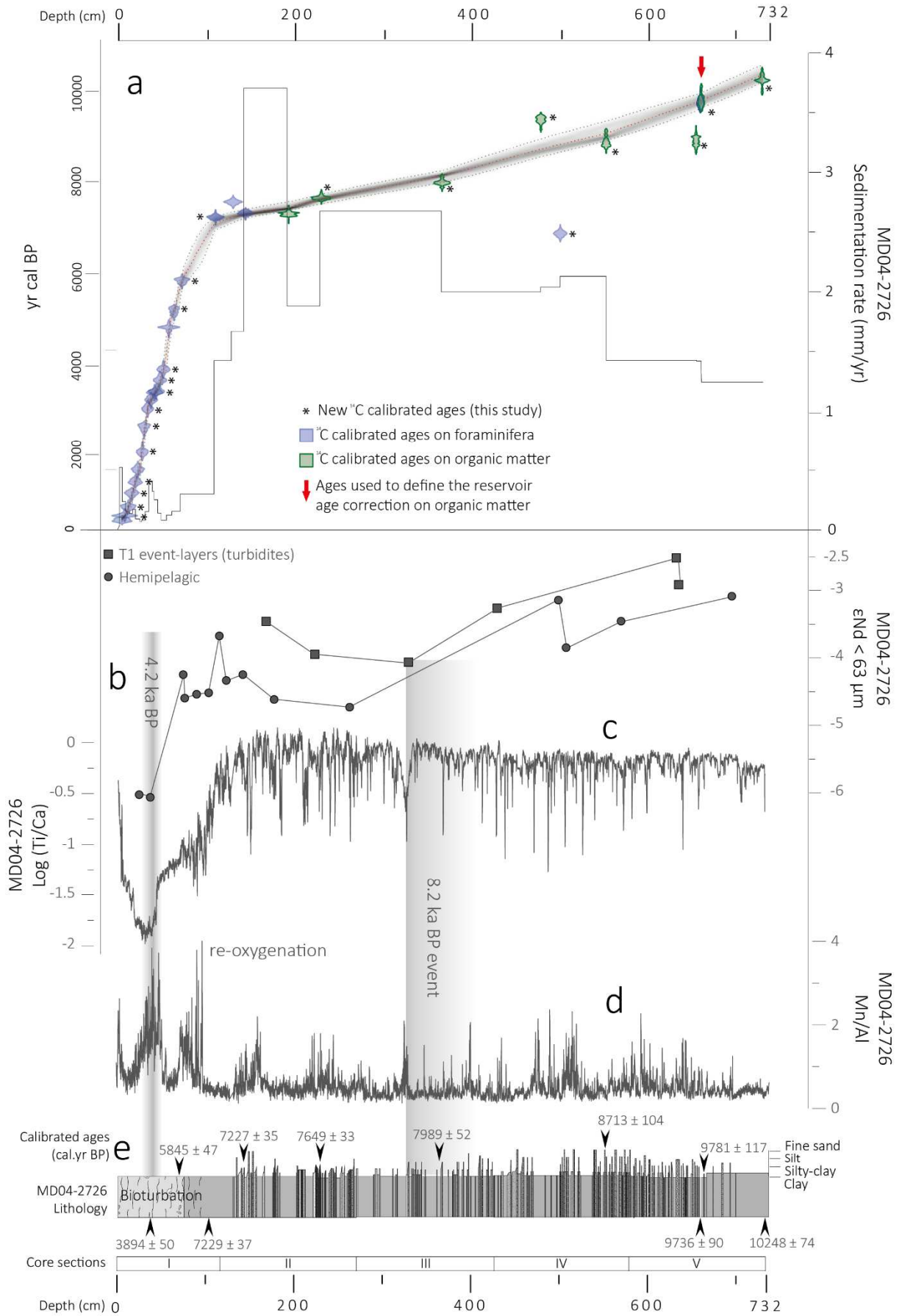
934 **Fig 2: a**) Age model of the MD04-2726 core with new (asterisk, this study), and previous (Revel et al.,

935 2015) ^{14}C calibrated ages, indicating ages obtained on foraminifera (blue tie points) and on organic

936 matter (green tie points); sedimentation rate (mm/yr) of the MD04-2726 core. **b**) Silt (<63 μm) εNd

937 values of T1 event-layers (squares) and hemipelagic sediments (dots) of the MD04-2726 core. **c**) Log

938 (Ti/Ca) and **d**) Mn/Al ratios from 1 mm resolution XRF core scanner measurements from the MD04-

939 2726 core. **e**) Lithology and texture of the MD04-2726 core with indicated section depths and the

940 localisation of new and previous calibrated ages.

941

942
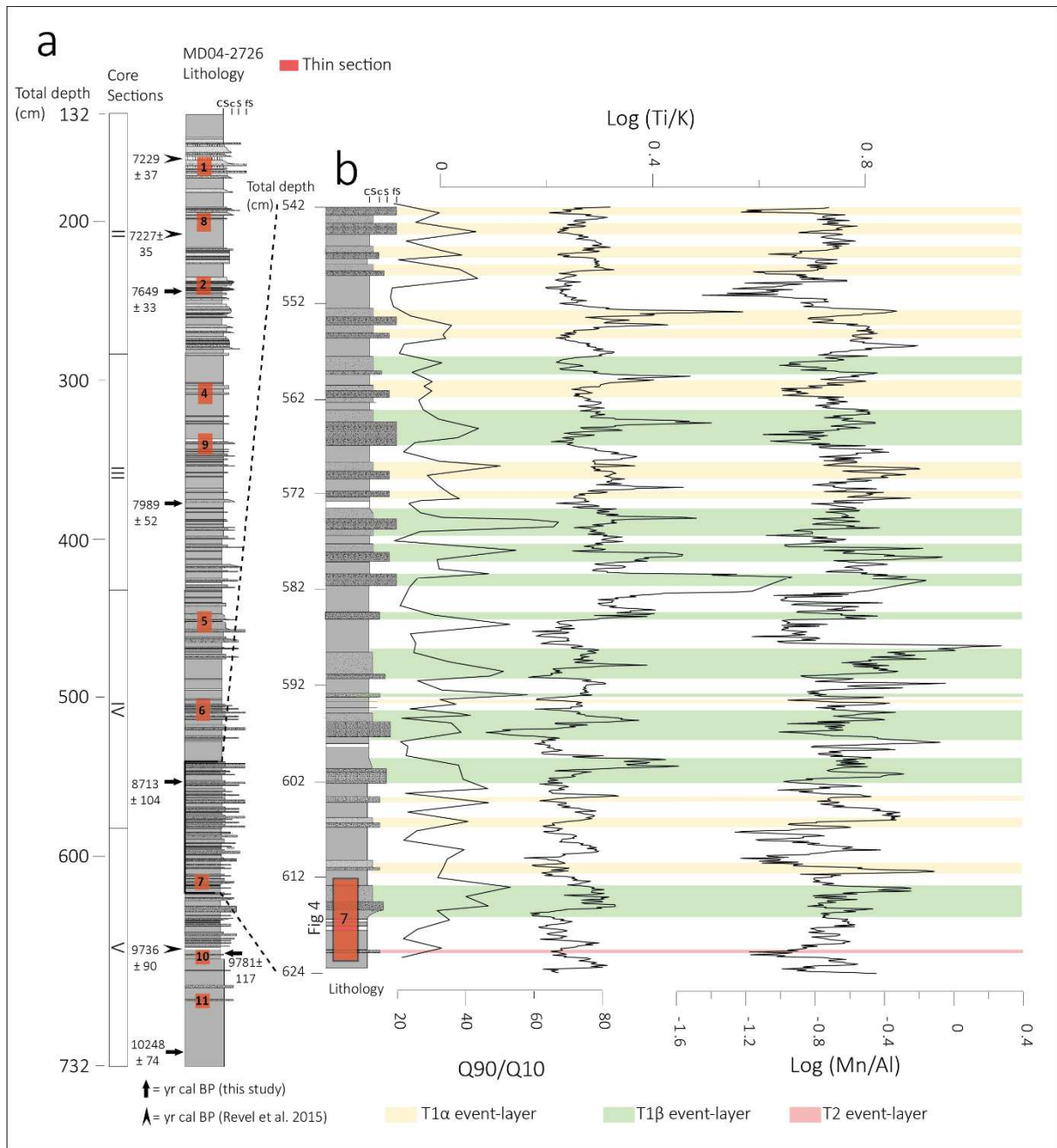
Fig 3: a) Lithology and texture of the turbidity sequence in core MD04-2726 (sections II to V), with the location of the sampled and studied thin sections (orange boxes) and of new and previous calibrated radiocarbon ages (see Fig. 2). b) Detail of the lithology for the interval 542 to 624 cm depth with the location of thin section N°7 (orange box, see Fig 4), the Q90/Q10 and Log(Ti/K) and Log(Mn/Al) ratios. The T1α, T1β and T2 event-layers are identified by yellow, green and red highlights, respectively.

948

949
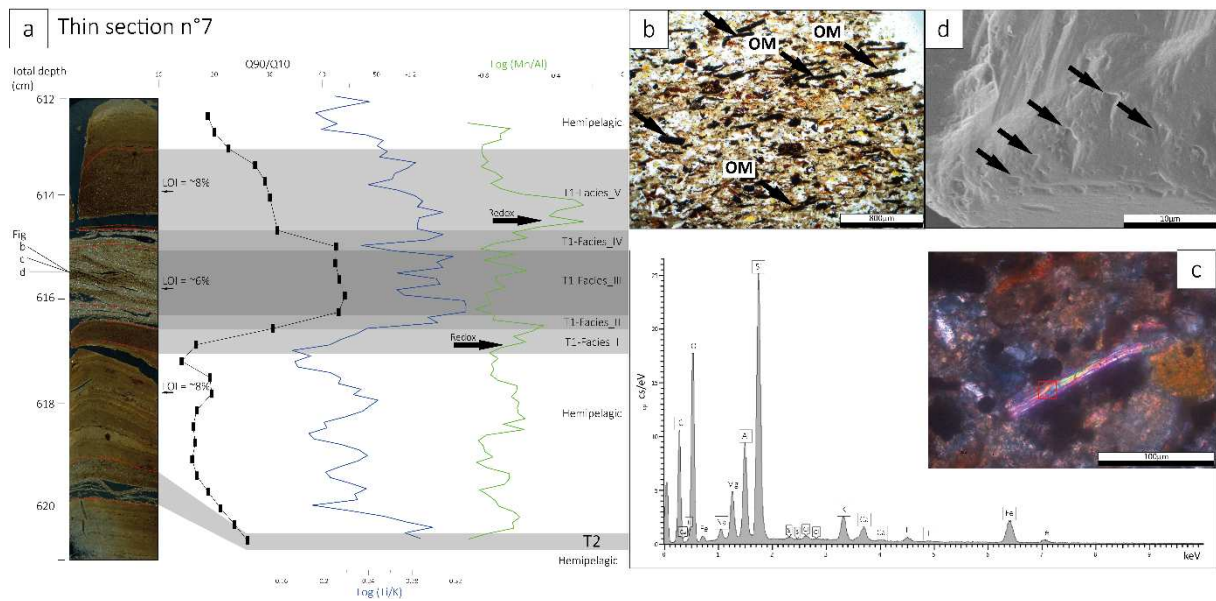
Fig 4: **a**) Scan in crossed polarized light of thin section N°7 with the location of Fig 4b, 4c and 4d, the T1 Facies (I to V), and the T2 and hemipelagic facies; Q90/Q10 (black line), Log(Ti/K) (blue line) and Log(Mn/Al) (green line); black arrows indicating the fluvial-induced redox facies; LOI (%) over hemipelagic and T1 sedimentary facies. **b**) SEM image in plane polarized light of T1 Facies III showing the organic matter (OM, black arrows) with horizontal orientation and distribution patterns in climbing ripple sedimentary patterns; **c**) SEM image in crossed polarized light of T1 Facies III showing a non-weathered mica mineral with the respective EDX analysis spectrum. **d**) SEM image of quartz grain surface showing small to large conchoidal microfractures and V–shaped percussion cracks (black arrows).

960
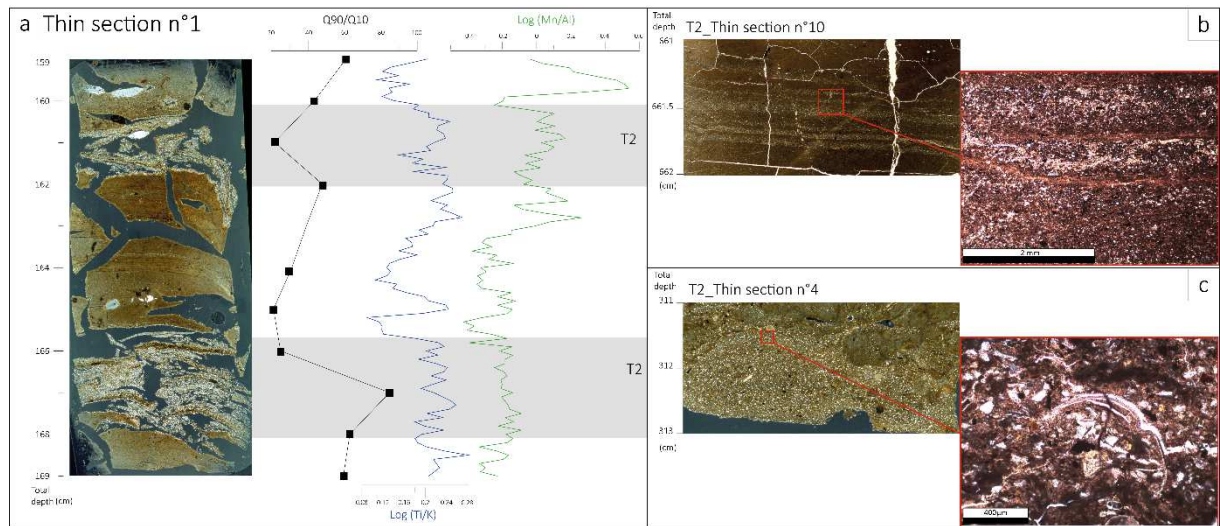
Fig 5: a) Scan in crossed polarized light of thin section N°1 with T2 event-layer facies locations and Log(Ti/K) (blue line), Log(Mn/Al) (green line) and Q90/Q10 (black line). b) Light microscopy and scan images in plane polarized light of T2 facies and localisation of thin section N°10, showing a massive deposition of silty beds. c) Light microscopy and scan images in plane polarized light of T2 facies and location of thin section N°4, showing massive and reworked sediment and a fragmented foraminifer.
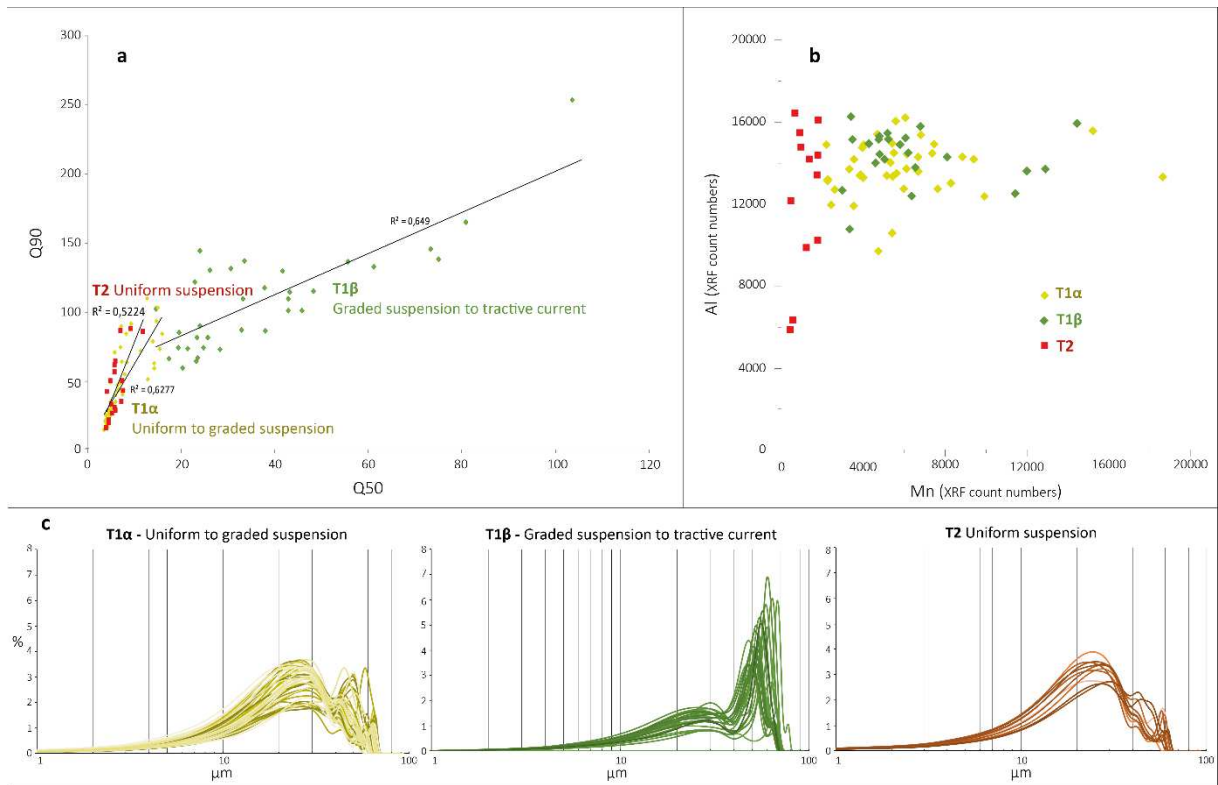
Fig 6: a) Q90 versus Q50 plot of all the T1 and T2 event-layers from MD04-2726 core, showing the distinction between T1α types suggesting a uniform to graded suspension, and T1β types suggesting a graded suspension to tractive current sedimentation mode and T2 event-layers indicating a uniform to graded suspension sedimentation mode. b) Mn/Al plot (XRF count numbers) of T1α, T1β and T2 event-layers from III-IV-V sections of MD04-2726 core; c) Grain-size distribution of T1α, T1β and T2 event-layers (volume percentage vs. log of grain-size in μm) showing the grain-size sorting effect of the different sedimentation processes.

978
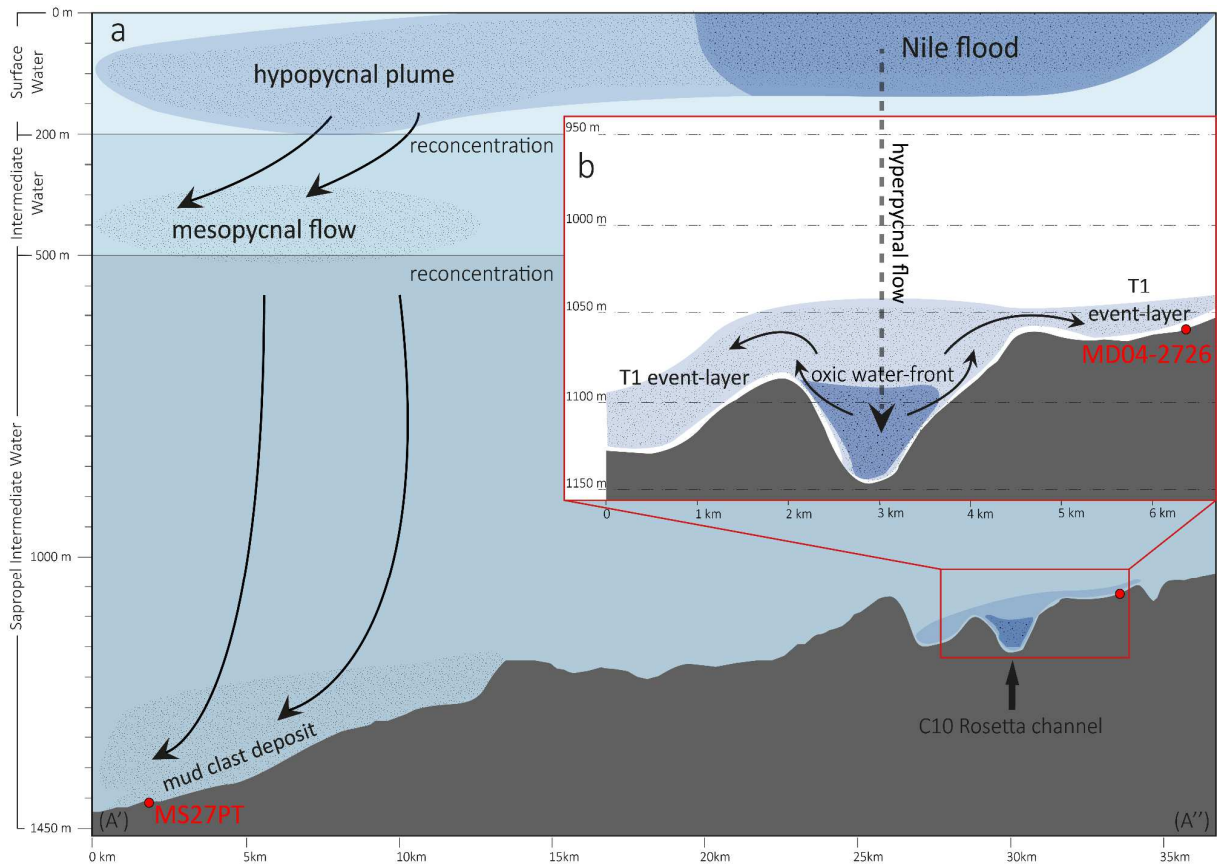
Fig 7: **a)** Bathymetric profile of the proximal Rosetta upper slope (A'-A'', shown in Fig 1a) with the
positions of the MD04-2726 and MS27PT cores; the Sapropel Intermediate Water, Intermediate
Water, Surface Water limits (after Zirks et al., 2019), and a schematic model of the formation process
of the mud clast deposits (after Ducassou et al., 2009). **b)** Detail of the bathymetric profile of the C10
Rosetta channel (shown in Fig 1a) with the position of the MD04-2726 core; and a schematic model of
the formation process of the T1 event-layers (this study).
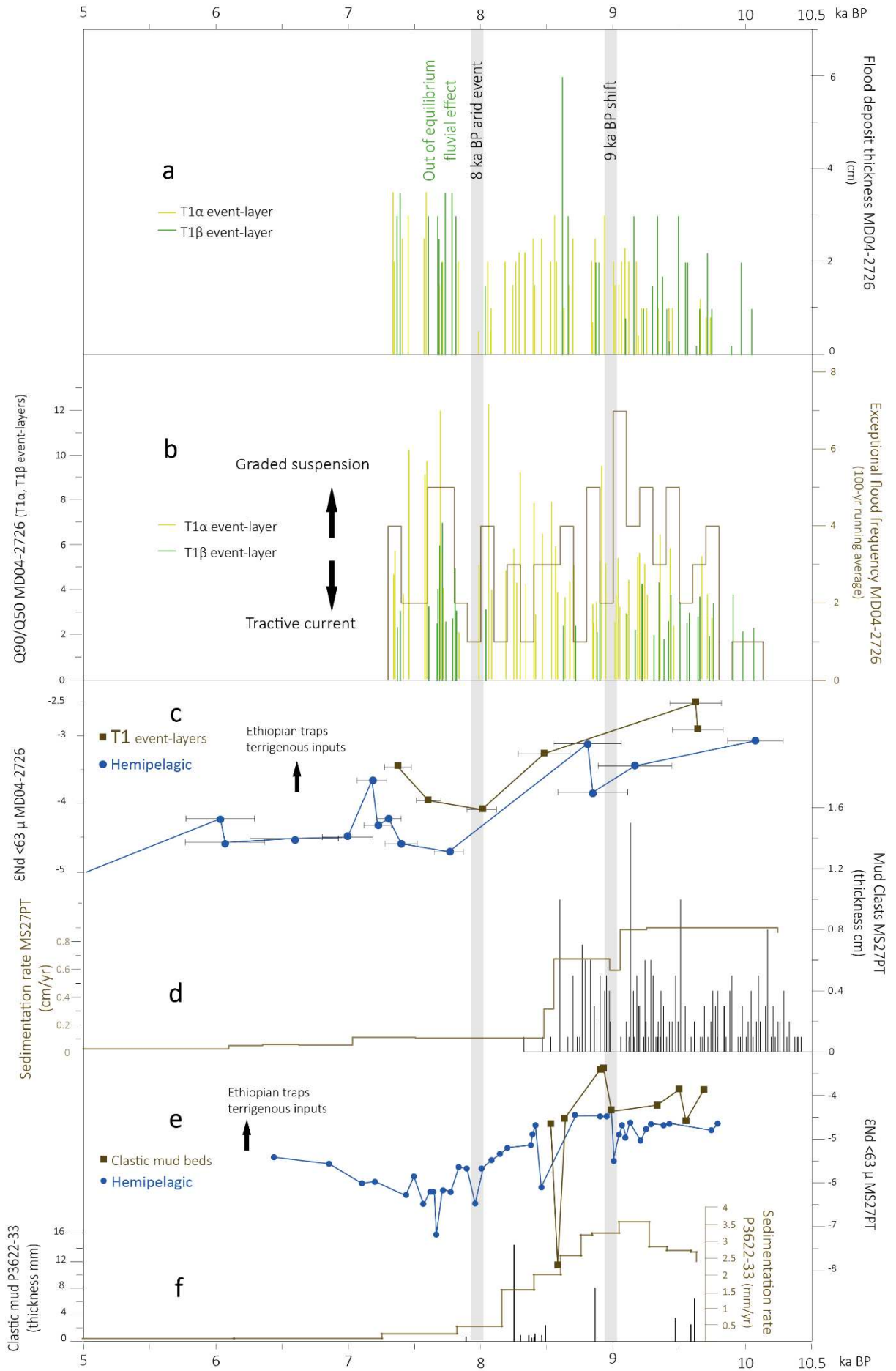
987   **Fig 8: a)** Thickness of flood-induced deposits (cm; T1α in yellow and T1β in green) of the MD04-2726

988   core. **b)** Q90/Q50 ratio and frequency (100-yr running average, brown line) of flood deposits (T1α in

989   yellow and T1β in green) of the MD04-2726 core. **c)** ƐNd of T1 event-layers (brown line and squares)

990   and hemipelagic sediment (blue line and dots). **d)** Sedimentation rate (cm/yr, brown line) and

991   thickness of mud clast deposits (T1α and T1β event-layers) of the MS27PT core. **e)** ƐNd of clastic mud

992   deposits (brown line and squares) and of hemipelagic sediment (blue line and dots) from core MS27PT

993   (fraction <63 μm; after Ménot et al., 2020; this study). **f)** Sedimentation rate (mm/yr, in brown) and

994   thickness of mud clast deposits from the P3622-33 core

995

996
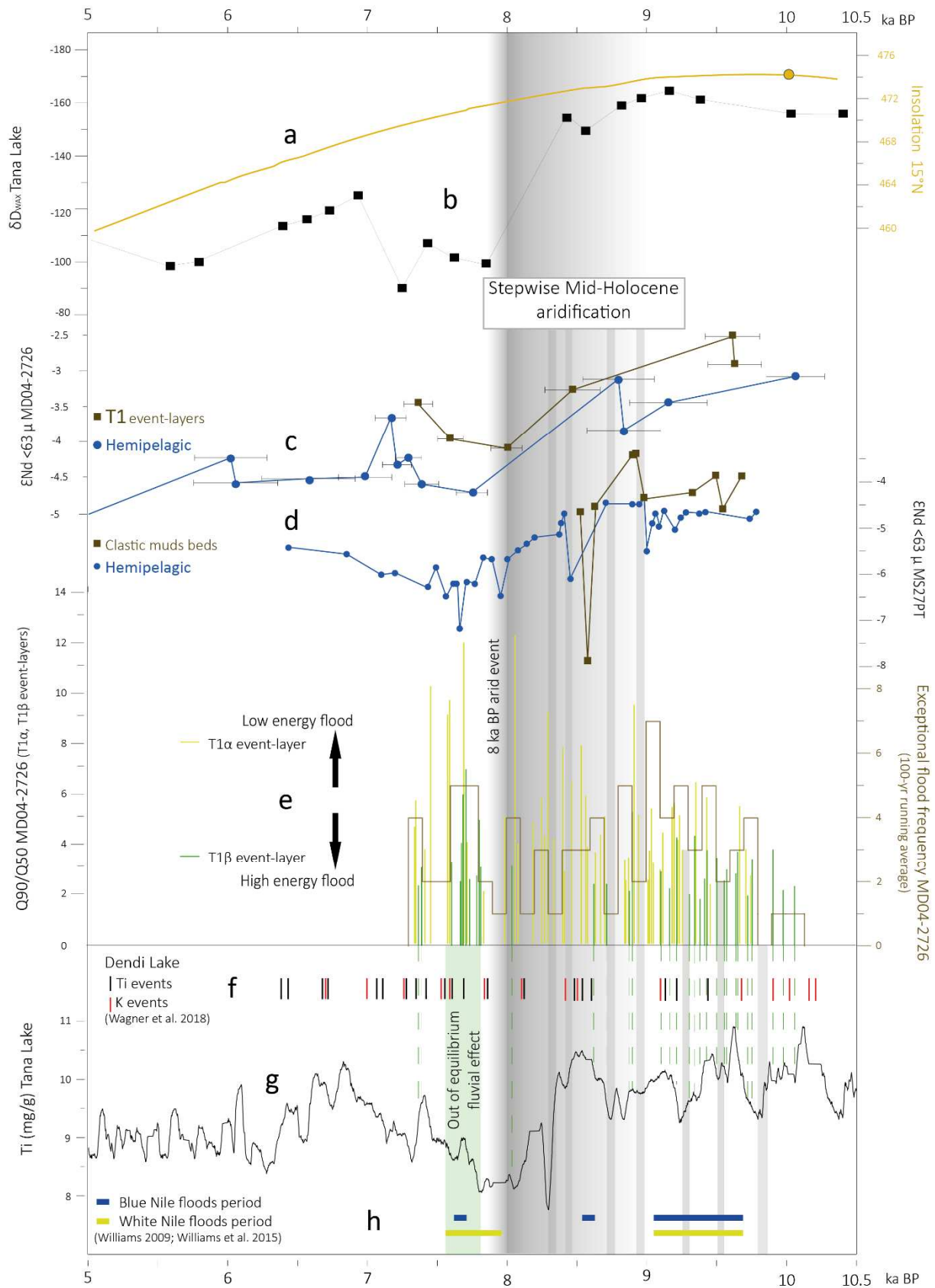
Fig 9: Paleovariations from 10.5 - 5 ka BP of: **a)** July insolation at 15°N (Berger and Loutre, 1991); **b)**

δD$_{WAX}$ (‰) at Lake Tana (Costa et al., 2014); **c)** εNd of T1 event-layers (brown line and squares) and

1000   hemipelagic sediment (blue line and points) of the MD04-2726 core; **d**) ƐNd of clastic mud deposits

1001   (brown line and squares) and of hemipelagic sediment (blue line and dots) from core MS27PT (fraction

1002   <63 µm) (after Ménot et al., 2020; this study) **e)** Q90/Q50 and frequency (100-yr running average,

1003   brown line) of exceptional flood deposits (T1α in yellow and T1β in green) of the MD04-2726 core; **f**)

1004   erosion runoff-induced K and Ti event layers from Lake Dendi (Wagner et al., 2018); **g**) Ti (mg/g) at

1005   Lake Tana (Marshall et al. 2011); **h**) Blue (in blue) and White (in yellow) lower Nile course flood periods

1006   recorded over the Karthoum region (Williams, 2009; Williams et al., 2015). Light grey bands indicate

1007   the lower flood frequency recorded in MD04-2726 core.

1008